

# JGR Solid Earth

## RESEARCH ARTICLE

10.1029/2023JB028241

### Key Points:

- This paper examines the shear velocity dependence of friction for dry granular materials, across nine orders of magnitude in shear velocity ( $10^{-8}$ –2 m/s)
- An “M-shaped” law for the variation of friction with velocity is obtained including two velocity-strengthening and two velocity-weakening laws
- There is microscopic evidence that ultra-high frequency vibration may cause high velocity shear weakening

### Supporting Information:

Supporting Information may be found in the online version of this article.

### Correspondence to:

W. Hu,  
huwei1999@126.com

### Citation:

Gou, H. X., Hu, W., Xu, Q., Chen, J., McSaveney, M. J., Breard, E. C. P., et al. (2024). Variation in granular frictional resistance across nine orders of magnitude in shear velocity. *Journal of Geophysical Research: Solid Earth*, 129, e2023JB028241. <https://doi.org/10.1029/2023JB028241>

Received 7 NOV 2023

Accepted 24 JUN 2024

### Author Contributions:

**Conceptualization:** H. X. Gou, W. Hu, Q. Xu, Jianye Chen, M. J. McSaveney, Eric C. P. Breard, R. Q. Huang

**Data curation:** Y. J. Wang

**Formal analysis:** H. X. Gou, W. Hu, Jianye Chen, R. Q. Huang, X. P. Jia, L. Zhou

**Investigation:** W. Hu, Jianye Chen, X. P. Jia

**Methodology:** W. Hu, Q. Xu, M. J. McSaveney

**Resources:** Y. J. Wang

**Software:** H. X. Gou, W. Hu, L. Zhou

**Supervision:** Eric C. P. Breard

**Validation:** W. Hu, Q. Xu,

M. J. McSaveney, Eric C. P. Breard, R. Q. Huang, L. Zhou

## Variation in Granular Frictional Resistance Across Nine Orders of Magnitude in Shear Velocity

H. X. Gou<sup>1</sup>, W. Hu<sup>1</sup> , Q. Xu<sup>1</sup>, Jianye Chen<sup>2</sup>, M. J. McSaveney<sup>1,3</sup> , Eric C. P. Breard<sup>4</sup>, R. Q. Huang<sup>1</sup>, Y. J. Wang<sup>5</sup>, X. P. Jia<sup>6</sup> , and L. Zhou<sup>1</sup>

<sup>1</sup>State Key Laboratory of Geo-Hazard Prevention and Geo-Environment Protection, Chengdu University of Technology, Chengdu, China, <sup>2</sup>Institute of Geology, China Earthquake Administration, Beijing, China, <sup>3</sup>GNS Science, Lower Hutt, New Zealand, <sup>4</sup>School of Geosciences, University of Edinburgh, Edinburgh, UK, <sup>5</sup>School of Physics and Astronomy, Shanghai Jiao Tong University, Shanghai, China, <sup>6</sup>Institut Langevin, ESPCI Paris, Université PSL, CNRS, Paris, France

**Abstract** Determining the shear-velocity dependence of dry granular friction can provide insight into the controlling variables in a dry granular friction law. Some laboratories believe that the quality of this study is at the forefront of the discipline for the following reasons. Results suggest that granular friction is greatly affected by shear-velocity ( $v$ ), but shear experiments over the large range of naturally occurring shear-velocities are lacking. Herein we examined the shear velocity dependence of dry friction for three granular materials, quartz sand, glass beads and fluorspar, across nine orders of magnitude of shear velocity ( $10^{-8}$ –2 m/s). Within this range, granular friction exhibited four regimes, following a broad approximate “m” shape including two velocity-strengthening and two velocity-weakening regimes. We discuss the possible physical mechanisms of each regime. This shear velocity dependence appeared to be universal for all particle types, shapes, sizes, and for all normal stresses over the tested range. We also found that ultra-high frequency vibration as grain surfaces were scoured by micro-chips were formed by spalling at high shear velocities, creating  $\sim 20\text{ }\mu\text{m}$  diameter impact pits on particle surfaces. This study provides laboratory laws of a friction-velocity ( $\mu$ - $v$ ) model for granular materials.

**Plain Language Summary** Numerous phenomena of earth science can be simplified to shearing granular systems, such as landslide gouge and rock avalanches. It is believed that friction varies with shear velocity, and this is no exception for dry granular materials. Studying the law of friction variation over as large a range of velocity changes as possible aids in establishing a full life-cycle hypothesis for landslides from initiation, through movement to cessation. We sheared granular materials across nine orders of magnitude, from  $10^{-8}$  to 2 m/s and obtained an “M” shape law for the variation of friction with velocity. By analyzing the acoustic frequency of shear experiments at different velocities, we discovered that the acoustic frequency increased with shear velocity. By comparing the microscopic morphology of the particle surface before and after high-velocity shearing, we hypothesized that the impact pits may be left by particle collisions during high-velocity shearing. We proposed that the role of ultra-high frequency vibration on high-velocity shear weakening should be considered, which provides a basis for accurately revealing the physical mechanism of granular friction variation with velocity.

## 1. Introduction

The frictional properties of granular flows have profound implications for the development of geological processes such as landslides and rock avalanches (Baumberger & Caroli, 2006; Hu et al., 2020, 2022; Jop et al., 2006; Kawamura et al., 2012; Marone, 1998; Melosh, 1996; Savage & Hutter, 1989; Scholz, 1998). In particular, the velocity dependence of the steady-state friction coefficient ( $\mu_{ss}$ ) of granular materials is indicative of the mechanisms underlying the life cycle of seismic faults and large landslides from initiation, through movement to cessation. Numerous velocity-dependent results of granular friction across small ranges of shear velocity in the laboratory showed that at very low shear velocities ( $v < 10^{-7}$  m/s), friction exhibits shear strengthening (Kuwano & Hatano, 2011; Shimamoto, 1986). At intermediate shear velocities (about  $10^{-7}$ – $10^{-5}$  m/s), granular friction displayed strain weakening (Bureau et al., 2002; Elst et al., 2012; Heslot et al., 1994; Kuwano et al., 2013; Reches & Lockner, 2010). At faster shear velocities (about  $10^{-5}$ – $10^{-1}$  m/s), granular friction shows strong shear strengthening (Bureau et al., 2002; Ferri et al., 2011; Heslot et al., 1994; Kuwano & Hatano, 2011; Kuwano et al., 2013; Reches & Lockner, 2010; Shimamoto, 1986; Taylor & Brodsky, 2017; Weeks, 1993). At even higher

shear velocities ( $v > 0.1$  m/s), profound shear weakening of granular friction is apparent (Chen et al., 2020; Di Toro et al., 2011; Ferri et al., 2011; Hu et al., 2020; Kohli et al., 2011; Reches & Lockner, 2010).

Many researchers have predicted shear-velocity dependence of granular friction based on a variety of physical models. For rock friction, researchers usually use a rate-and-state friction law (RSF) to explain the shear-velocity dependence of friction (Dieterich, 1979; Marone, 1998; Ruina, 1983; Scholz, 1998). For granular materials, researchers considered granular friction from particle interactions at different shear velocities. At different shear velocities, the description of a granular flow can range from “solid-like” to “gas-like” (Bagnold, 1954; Campbell, 2005; Jaeger et al., 1996). The concept of a dimensionless inertial number ( $I$ ) was used to describe the grain inertial stress in the confining stress (Bocquet et al., 2001; Campbell, 2006; Clement, 1999; GDRMiDi, 2004; Iverson, 1997; Lu et al., 2007; Savage, 1984).

$$I = \frac{\dot{\gamma}d}{\sqrt{P/\rho}} \quad (1)$$

where  $\dot{\gamma}$  is the shear strain rate,  $P$  is the normal stress,  $\rho$  is the grain density, and  $d$  is the grain diameter. Rabinowicz (1951) hypothesized that dry granular friction was controlled by the area ( $A_r$ ) of the ensemble of asperities between two contacting macroscopic bodies, which depended on the elapsed time after forming a contact, also called the contact’s “maturity” or “age.” We can use a time dimension state variable  $\phi$  to quantify it (Baumberger & Caroli, 2006; Dieterich, 1978; Dieterich & Kilgore, 1994; Rice et al., 2001; Ruina, 1983). As this hypothesis evolves, it is suggested that the frictional resistance ( $\tau$ ) is directly related to  $A_r(\phi)$  (Bowden & Tabor, 1964). Furthermore, the shear strain rate ( $\dot{\gamma}$ ) has the potential to influence the scaling factor and a collection of internal state variables symbolized as  $\theta$ . These variables can be represented diagrammatically as the shear resistance denoted by  $\sigma_s(\theta, \dot{\gamma})$  (Baumberger & Caroli, 2006; Bowden & Tabor, 1964). Then the  $\tau^{ss}(\dot{\gamma})$  (steady-state frictional resistance) can be expressed as:

$$\tau^{ss}(\dot{\gamma}) = \frac{A_r[\phi(\dot{\gamma})]\sigma_s[\theta(\dot{\gamma}), \dot{\gamma}]}{A_n} \quad (2)$$

where  $A_n$  is the nominal contact area.

The transitions in the velocity dependence of shear strength as described above have also been the focus of various empirical or micromechanical friction laws (Chester & Higgs, 1992; Noda & Shimamoto, 2010; Putelat et al., 2007; Reinen et al., 1992). A microphysical model based on carbonate faults, which takes into account the porosity of the principal slip zone (PSZ) and temperature variations is known as the “Chen-Niemeijer-Spiers” (CNS) model, and is currently in good agreement with the velocity dependence of friction across a large range of laboratory shear velocities. The model is proposed in Chen and Spiers (2016) and can approximately describe the velocity dependence of granular friction considering creep, shear velocity, and temperature after further refinement (Chen & Spiers, 2016; Chen & Niemeijer, 2017a; Chen et al., 2017, 2020). Aharonov and Scholz (2018) have recently established a physics-derived principle governing rock friction that takes into account the microphysics of contact creep, incorporates an exponential law, and accounts for the interaction between frictional heating and the process. Their model examines the stress and temperature levels at asperities, and it can forecast various deformation modes based on velocity, including local (flash) melting.

The velocity-dependence of friction for granular materials across the possible large range of shear velocities still requires verification. Previous researchers have studied small and scattered shear-velocity ranges which were less than 5 orders of magnitude. In this study, we described velocity-dependent experiments on granular friction across 9 orders of magnitude in shear velocity ( $10^{-8}$ – $2$  m/s) for three kinds of granular materials. Our results appeared to be in good agreement with the latest Chen et al. (2020) model. In addition, we recorded acoustic emissions to investigate factors other than temperature that led to weakening at high shear velocities, leading us to suggest that shear-induced internal vibration may also contribute to weakening.

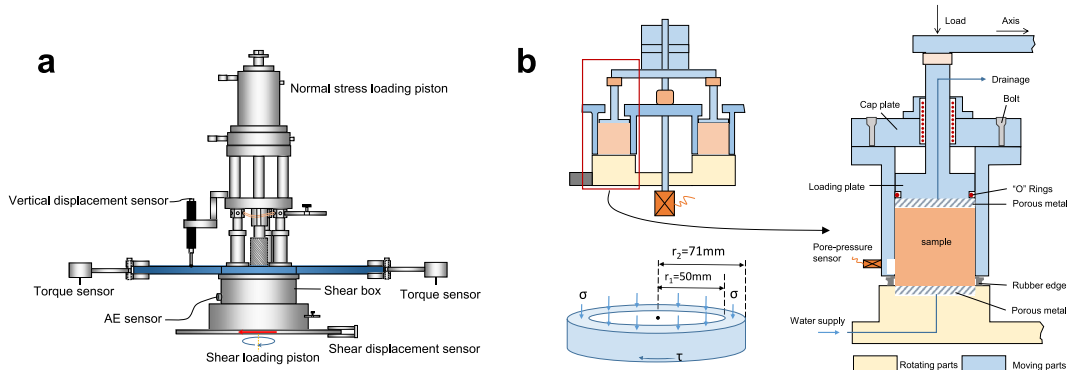


**Figure 1.** (a) Schematic diagram of the mechanical components of the ICL apparatus, position of the acoustic sensor and the size of sample. (b) Cross section of the entire specimen configuration and the details of a cross-section of the shear box, and the model diagram of distribution of normal stress ( $\sigma$ ) and shear stress ( $\tau$ ) of the whole sample.

## 2. Method

### 2.1. Material and Description of the Apparatus

Herein we compare the mechanical properties of granular materials under different conditions. Shear velocity differs across 9 orders of magnitude ( $10^{-8}$ – $2$  m/s). We used different granular materials: glass beads (specific gravity of 2.60), quartz sand (specific gravity of 2.65), and fluorspar (specific gravity of 3.18). Fluorspar is commonly found in various geological environments, including hydrothermal veins, sedimentary rocks, and hot spring deposits. Fluorspar has a hardness of 4 on the Mohs scale, so it is relatively softer compared to many other minerals. This softness can make fluorite susceptible to scratching and damage. Different grain diameters: 0.2, 0.5, 0.8, and 1.0 mm were selected, and different normal stresses were applied: 200, 500, and 1,000 kPa. Experiments across this shear-velocity range were carried out using a rotary-shear International Consortium on Landslides (ICL) apparatus (Figure 1a) and the Low-to-High Velocity Rotary-shear (LHVR) apparatus (Figure 2a), covering the slow and rapid velocity ranges, respectively ( $10^{-8}$ – $0.5$  m/s in the ICL apparatus and  $10^{-4}$ – $2$  m/s in the LHVR apparatus).

We followed the methods of, Johnson and Jia (2005), Johnson and Jia (2005), Jop et al. (2006), Savage and Marone (2008), Elst et al. (2012), and Kuwano et al. (2013) to use glass beads packs as a simplified granular material that avoids particle shape, particle crushing and other factors, which may reflect the physical mechanisms of geological shear zones. A second advantage of uniform granular beads is that they allow simple, accurate analysis of changes in grain morphology (Rossi et al., 2007; Scuderi et al., 2015). Finally, spherical beads are commonly used in numerical simulations, which is the focus of ongoing work (Ferdousi et al., 2014).

Acoustic emissions were recorded continuously during the experiments. We used wide-band acoustic sensors (WD type,  $\varphi 18\text{ mm} \times 17\text{ mm}$ , made by Physical Acoustics Corporation, USA). The maximum frequency of the AE signal that can be captured (Peak Frequency) is 900 kHz. AE sensors were attached on both ICL and LHVR apparatuses, and the data were collected at a frequency of 1 MHz using commercial acquisition systems (National Apparatus Company, USA, NI compact DQA, PXIe-1084 and BNC-2110). The attachment point of the AE sensor on the two apparatuses is shown in Figures 1a and 2b respectively.

After high-velocity shearing, the grain texture and surface were examined at high magnification using a scanning electron microscopy (SEM). The change of surface roughness after high-velocity shearing was measured by a Confocal Microscope (UP-Lambda, made by Rtec Instruments, USA). The information on the experiments performed is summarized in Table 1. After the experiments, we sieved samples of quartz sand and fluorspar and discovered that both of them were crushed, while the glass beads remained at a uniform grain diameter.

### 2.2. Slow Shear Experiments

The slow shear experiments described in this study were carried out using the ICL ring shear apparatus (Figure 1a, described in Sassa et al. (2014)). The ring-shaped shear box had an inner diameter ( $r_1$ ) of 71 mm, an outer diameter ( $r_2$ ) of 50 mm, and the height of the sample involved in shearing was about 13 mm ( $h$ ). The cross-section

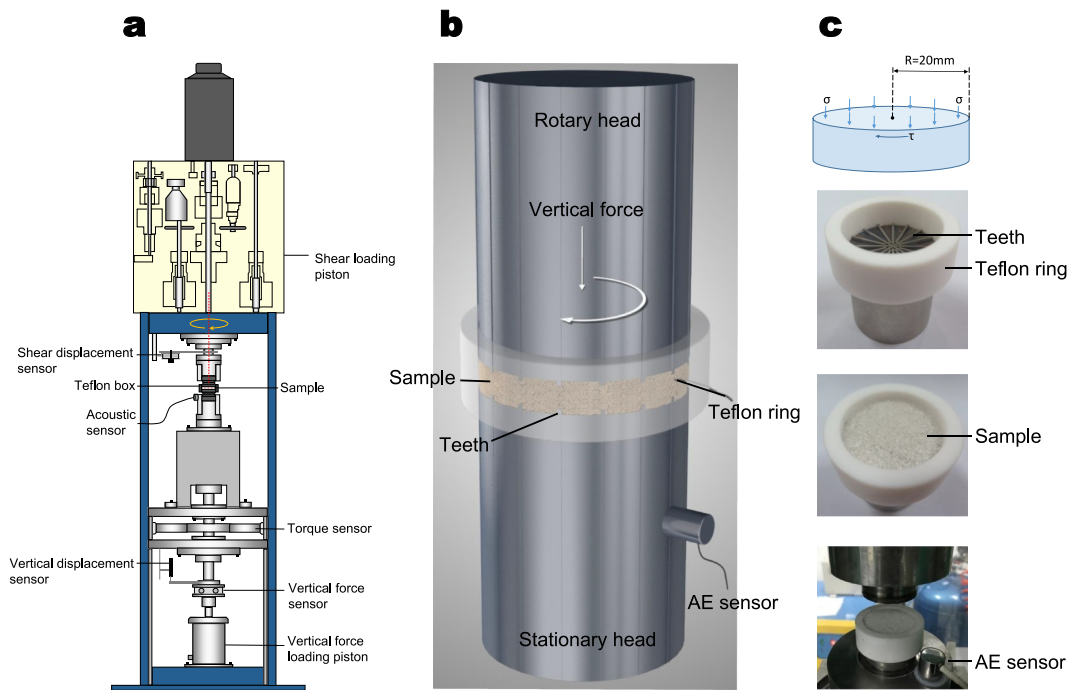


**Figure 2.** (a) The mechanical components of the LHVR are depicted in a schematic diagram. (b) The modified sample loading mode and position of the AE sensor (the detail was shown as Movie S1). (c) A model diagram of the distribution of normal stress ( $\sigma$ ) and shear stress ( $\tau$ ) of the whole sample and loading process of granular material samples.

of the entire specimen configuration and the details of a cross-section of the shear box are shown in Figure 1b. The upper part (moving part) was fixed during shearing, and the specimen was sheared by rotating the lower part (rotating part). The shear resistance was measured by two torque sensors attached to the upper part. Rubber rings were glued to the lower part of the shear box at the joint to prevent unintended leakage during consolidation and

**Table 1**  
*Table of the Experiments Performed in the ICL and LHVR*

Set no.	Apparatus	Material	Diameter (mm)	Normal stress (kPa)	Velocity (m/s)
1	ICL	Glass bead	0.2	200	$10^{-8}$ –0.5
2	ICL	Glass bead	0.2	500	$10^{-8}$ –0.5
3	ICL	Glass bead	0.2	1,000	$10^{-8}$ –0.5
4	ICL	Quartz sand	1	200	$10^{-8}$ –0.5
5	ICL	Quartz sand	1	500	$10^{-8}$ –0.5
6	ICL	Quartz sand	1	1,000	$10^{-8}$ –0.5
7	ICL	Fluorspar	1	500	$10^{-8}$ –0.5
8	ICL	Fluorspar	1	1,000	$10^{-8}$ –0.5
9	LHVR	Glass bead	0.2	500	$10^{-4}$ –2.0
10	LHVR	Glass bead	0.2	1,000	$10^{-4}$ –2.0
11	LHVR	Glass bead	0.5	1,000	$10^{-4}$ –2.0
12	LHVR	Glass bead	0.8	1,000	$10^{-4}$ –2.0
13	LHVR	Glass bead	1.0	1,000	$10^{-4}$ –2.0
14	LHVR	Quartz sand	1.0	500	$10^{-4}$ –2.0
15	LHVR	Quartz sand	1.0	1,000	$10^{-4}$ –2.0
16	LHVR	Fluorspar	1.0	1,000	$10^{-4}$ –2.0

shearing. The distribution of normal stress ( $\sigma$ ) and shear stress ( $\tau$ ) of the whole sample is shown in the model diagram in Figure 1b. The apparatus can be used to perform velocity-controlled and torque-controlled tests with an applied maximum normal stress of 3 MPa and a maximum shear velocity of 0.5 m/s. The precision of the normal stress load sensor and shear load sensor is 0.01%–0.03% of full scale. For the shear-velocity control, the lower part of the shear box was rotated using a servo-controlled ram at different constant angular velocities. We used the average of the inner and outer diameter of the annular sample as the equivalent radius to calculate the shear velocity (Jiang et al., 2017; Sassa et al., 2014).

For the granular layer to shear freely as in a natural rock avalanche, the “Bromhead” mode was employed to simulate granular kinematics without a forced shear plane (Bromhead, 1979). Since the ICL apparatus has a circle width of about 20 mm, for the glass beads, we thought that the grain size should be less than 1/10 of the sample size, so we chose 0.2 mm grains. For the quartz sand, we wanted to be consistent with the grain size of the LHV sample, so we chose 1 mm grains. One mm of quartz sand can produce significant crushing. Experiments were carried out with 0.2 mm glass beads and 1 mm quartz sand under three normal stresses (200, 500, and 1,000 kPa). The shear velocities performed on the ICL ranged from  $10^{-8}$  to 0.5 m/s. Twenty-six experiments with different velocities were performed across this range.

### 2.3. Rapid Shear Experiments

We did the rapid shear experiments using the low-to-high rotary-shear apparatus (LHVR), which was installed at the Institute of Geology, China Earthquake Administration (Ma et al., 2014) (Figure 2a). The apparatus can be used for velocity-controlled and torque-controlled tests with applied maximum normal stresses up to 80 MPa and a maximum nominal shear velocity of 2 m/s. We modified the original loading method of the LHVR to achieve high-velocity shearing of thick granular material samples. The assembly method of the modified sample is shown in Figure 2b. To prevent any relative sliding of the interfaces between the particles and the loading heads, teeth measuring 1 mm in height were attached on the upper and lower loading heads, and the sample thickness was raised from 1 mm (as outlined in Ma et al. (2014)) to around 10 mm. The loading head was made of titanium alloy. We restricted the granular materials using a hollow Teflon cylinder with a diameter of ~40 mm and a thickness of ~9 mm and a thermocouple was set up to monitor the sample temperature (Hu et al., 2022) (Figure 2c). It was assumed that shear stress was a constant in the circular region and the average velocity of the radius distribution of the contact circle between the rotary head and the sample was the shear velocity (Di Toro et al., 2004; Shimamoto & Tsutsumi, 1994). We added an assumption that about 9 mm thick samples were all involved in shear to calculate the shear strain rate ( $\dot{\gamma}$ ) in this study.

We also used the “Bromhead” mode to simulate granular kinematics without a forced shear plane (Bromhead, 1979). The experiments were performed at a 1,000 kPa normal stress on four sizes of glass beads (0.2, 0.5, 0.8, and 1.0 mm) and 1 mm quartz sand, and fluorspar. The shear velocities performed on the LHVR ranged from  $10^{-4}$  to 2 m/s. Ten experiments of different velocity were performed across this range.

### 2.4. Calculation of Shear Velocity and Shear Stress

For both slow (ICL) and rapid shear tests (LHVR), we followed the same method to calculate shear velocity and shear stress. The shear velocity  $v$  changes depending on the radial location of the cylinder. To calculate an equivalent shear velocity, denoted as  $\tau v e S$ , which describes the rate of total frictional work on the shear surface area  $S$ , we adopted the approach of Shimamoto and Tsutsumi (1994) and Hirose and Shimamoto (2005). The  $v$  can be calculated as:

$$v = \frac{4\pi R(r_1^2 + r_1 r_2 + r_2^2)}{3(r_1 + r_2)} \quad (3)$$

In this study, the revolution rate of the motor is denoted by  $R$ , while  $r_1$  and  $r_2$  represent the inner and outer diameters of the hollow cylindrical specimens. It should be noted that in the context of rapid tests involving a solid cylinder (LHVR), the value of  $r_1$  is considered to be zero, so we get

$$v = \frac{4\pi R r_2}{3} \quad (4)$$

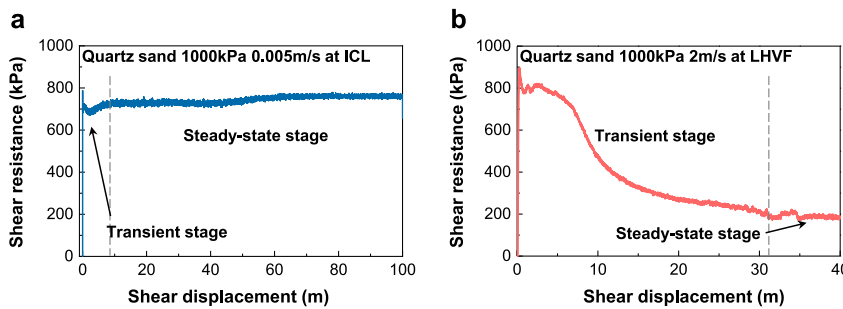


**Figure 3.** The division of the transient stage and steady-state stage. (a) Mechanical results of quartz sand at 1,000 kPa at 0.005 m/s in the ICL apparatus. (b) Mechanical results of quartz sand at 1,000 kPa at 2 m/s in the LHVF apparatus.

We also assume that for a uniform shear stress  $\tau$  over the sliding surface, torque  $T$  is given by:

$$T = \frac{2\pi\tau}{3}(r_2^3 - r_1^3) \quad (5)$$

for rapid tests with a solid cylinder (LHVR),  $T = 2\pi\tau r^3$ .

## 2.5. Determination of Steady-State and Modification of the ICL Friction Coefficient

We sheared the experiments at different velocity conditions for a sufficient distance that the shear resistance remained essentially stable. We followed Di Toro et al. (2004) to divide the shear process into a “transient stage” and a “steady-state stage,” as shown in Figure 3. In the transient stage, the shear strength varied (including weakening, as in Figure 3b) to relatively stable values in the steady-state stage. We observed that the characteristic distance of the transient stage increased with increasing shear velocity, but it is not within the scope of the present study. The ratio of the steady-state shear resistance ( $\tau_{ss}$ ) to the normal stress ( $\sigma$ ) was taken as the steady-state friction coefficient ( $\mu_{ss}$ ). In this study, we focused on the dependence of the steady-state friction coefficient on the shear velocity.

Experiments performed on these two rotary shear devices had overlapping shear velocities. However, even when the same materials were sheared at the same velocity under the same normal stress, we obtained significantly different  $\mu_{ss}$  values. What we measured was all friction, which included boundary friction. In general,  $\mu_{ss}$  of experiments performed on the ICL apparatus was larger than that on the LHVR under the same conditions, because the sidewall material of the ICL apparatus was stainless steel (sliding friction coefficient is 0.3–0.4) and the sidewall material of the LHVR apparatus was Teflon (sliding friction coefficient is 0.05). In this study, the boundary friction caused by the sidewall made of Teflon was ignored. The friction measured in the ICL apparatus consisted of three components: friction inside the shear granular layer ( $\mu$ ), friction between the granular and the inner and outer ring boundary walls of the shear box ( $\mu_b$ ), and friction between the shear box and the rubber ring ( $\mu_r$ ). We have corrected the friction coefficient obtained from the ICL apparatus using the following equation:

$$\mu = \mu_0 - \mu_b - \mu_r \quad (6)$$

where  $\mu_0$  is the friction coefficient measured directly by the ICL apparatus. We calibrated  $\mu_r$  by shearing water at 200, 500, and 1,000 kPa for 25, 20, and 15 kPa, respectively. We calculated  $\mu_b$  using the following equation:

$$\mu_b = \frac{T_b}{T_0} \mu_0 = \frac{2\pi r_1 h \cdot k\sigma \cdot \mu_x \cdot r_1 + 2\pi r_2 h \cdot k\sigma \cdot \mu_x \cdot r_2}{T_0} \cdot \mu_0 \quad (7)$$

where  $T_b$  is the sidewall friction additional torque, and  $e$  is the total measured torque of ICL.  $k$  is the ratio of lateral pressure to vertical pressure, taking  $k = 0.5$  (Sassa et al., 2014),  $h$  is the sample height involved in shear,  $\sigma$  is the normal stress,  $\mu_x$  is the sliding friction coefficient between the granular material and the stainless-steel side wall (rolling friction and dependence of  $\mu_x$  on shear velocity were not considered here), and  $r_1$  and  $r_2$  are the inner and outer diameters of the shear box, respectively.

The porosity was calculated by dividing the particle volume by the sample volume. We used the difference between the maximum and average values of the shear resistance at the steady-state stage as the experimental error bar.

### 3. Results

#### 3.1. Slow Shear Experiments

We measured the mechanical properties of the granular materials in the ICL apparatus across as wide a range of shear velocities as was possible. We selected two materials, glass beads and quartz sand, and three normal stresses of 200, 500, and 1,000 kPa. The detailed mechanical results of 1 mm quartz sand under 1,000 kPa at ICL is shown in Figure 4, which shows the variations in shear resistance and porosity during shear recorded by the ICL apparatus at 26 velocities in the range of  $10^{-8}$ –0.5 m/s. The detailed mechanical results of quartz sand and glass beads under different experimental conditions are shown in Figures S1–S5 of the Supporting Information S1.

Based on the results of Figure 4 and Figures S1–S5 in Supporting Information S1 we calculated the steady-state friction coefficients at different velocities and modified them based on Equations 6 and 7. The dependence of the modified steady-state friction coefficient ( $\mu_{ss}$ ) and steady-state porosity ( $V_{ss}$ ) of quartz sand and glass beads on the velocity is shown in Figure 5. The experimental results for glass beads are shown in Figure 5a. With the increase of velocity, the trend in  $\mu_{ss}$  increased by 0.1 in the velocity range of  $10^{-8}$ – $10^{-7}$  m/s, decreased by 0.2 in the velocity range of  $10^{-7}$ – $10^{-5}$  m/s, and increased again by 0.1 in the velocity range of  $10^{-5}$ – $10^{-1}$  m/s. When the velocity was extremely low ( $v < 10^{-7}$  m/s), we found that the  $\mu_{ss}$  of glass beads was also influenced by normal stress: the higher the normal stress, the lower the  $\mu_{ss}$ . After that, with increase in velocity,  $\mu_{ss}$  curves under the three normal stresses gradually approached until they overlapped.

The results for quartz sand are shown in Figure 5c. The steady-state friction coefficient showed similar trends for glass beads, but the  $\mu_{ss}$  of quartz sand was more influenced by normal stress. For extremely low velocities ( $v < 10^{-7}$  m/s), the higher the normal stress, the lower the  $\mu_{ss}$ . As velocity increased, the  $\mu_{ss}$  curves became steeper in the descending section and gentler in the second ascending section with increasing normal stress. In particular,  $\mu_{ss}$  showed a second slight decreasing trend at high shear velocities ( $v > 0.1$  m/s) at 1,000 kPa. The porosity changes of two materials at different shear velocities were shown in Figures 5b and 5d, and the  $V_{ss}$  gradually became smaller with increasing velocity. The higher the normal stress, the more obvious the shear contraction.

Experimental results from ICL showed that both glass beads and quartz sand exhibited a pattern of  $\mu_{ss}$  increasing, decreasing, and then increasing with increasing velocity. In particular, there was a second slight weakening of quartz sand when  $v > 0.1$  m/s at 1,000 kPa. A bit of  $v$ -weakening results for quartz sand can only be obtained (Figure 5b) at high shear velocity ( $v > 0.1$  m/s) due to the maximum shear velocity of the ICL apparatus being 0.5 m/s. Fluorspar, a more easily crushed material, was used for further experiments: it showed a more pronounced rapid-shear weakening on the ICL apparatus (Figure 6). In the variation pattern of  $\mu_{ss}$  the velocity for fluorspar was also similar for different normal stresses for 500 and 1,000 kPa (Figure 6). The individual mechanical data of fluorspar under different experimental conditions is shown in Figures S6 and S7 of the Supporting Information S1.

#### 3.2. Rapid-Shear Experiments

##### 3.2.1. Mechanical Data

Since the maximum shear velocity in the ICL apparatus is 0.5 m/s, we used the LHVR apparatus to study the frictional characteristics of the granular materials at higher shear velocities. The normal stress for these experiments was set at 1,000 kPa.

The detailed mechanical results of LHVR tests with different size of glass beads are shown in Figure 7. The test results on the left side (Figures 7a, 7c, 7e, and 7g) represented the mechanical results with shearing velocities from 0.0001 to 0.07 m/s for different sizes of glass beads (from 0.2 to 1 mm). No evident weakening was observed in those results. If we increased the velocity to the range from 0.1 to 2 m/s, the shear resistance weakening became very evident, as shown in the right side of Figure 7 (Figures 7b, 7d, 7f, and 7h). Moreover, no crushing was observed after the rapid shearing for all the glass bead tests. From shear velocities of 0.1 to 2 m/s (comparatively high speed), the glass beads of different sizes presented different initial friction coefficients, however the steady-

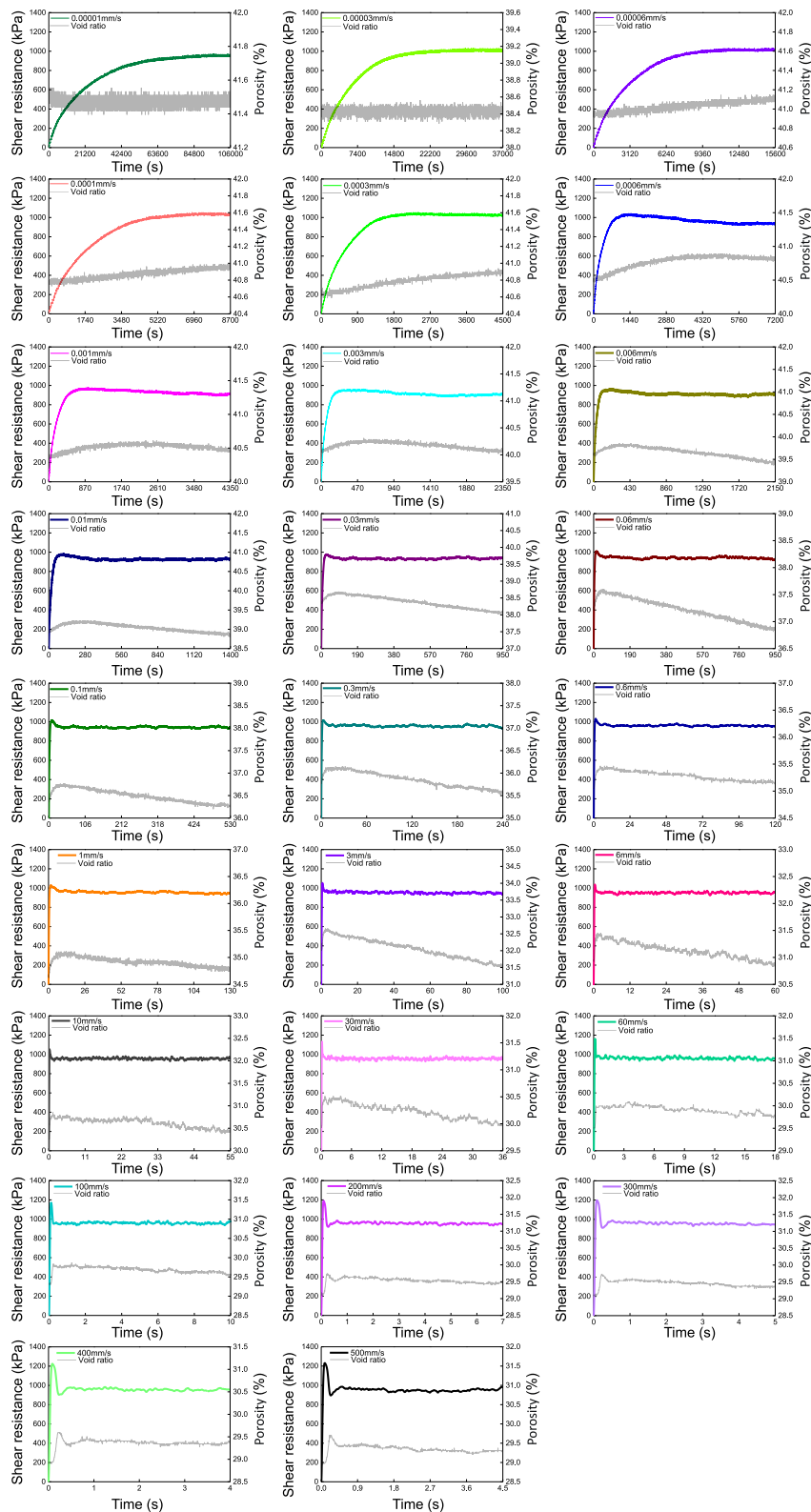


**Figure 4.** Mechanical results of for each velocity at using 1 mm quartz sand at 1,000 kPa on the ICL apparatus.

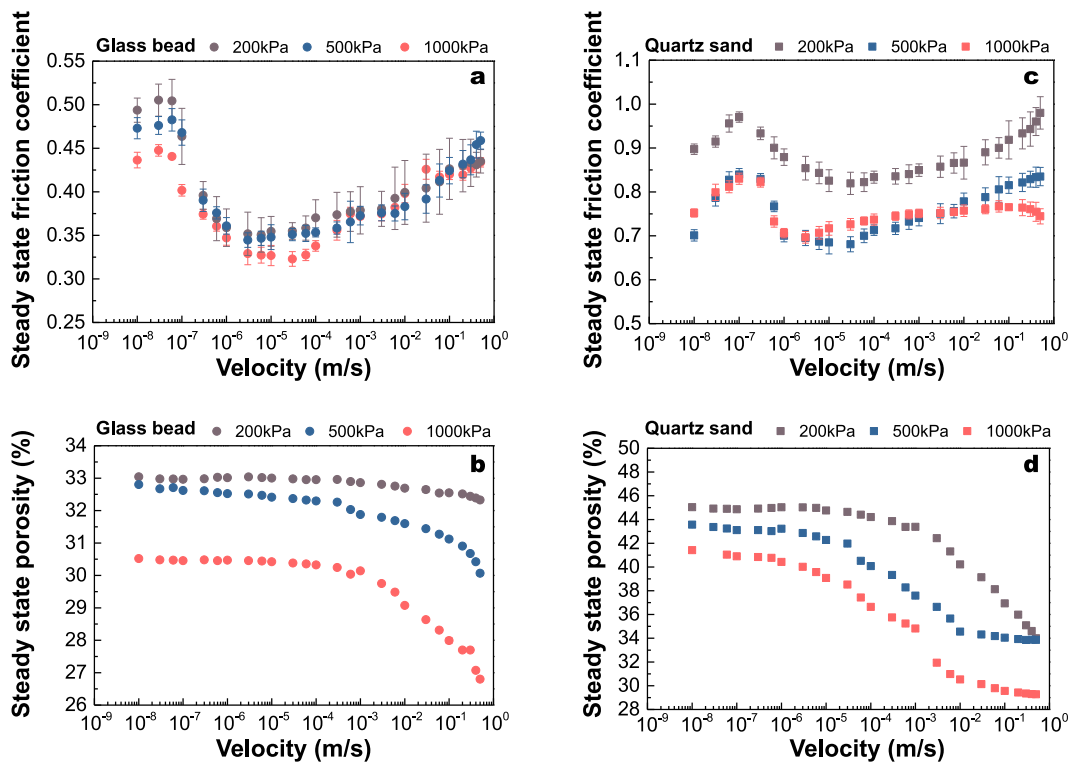


**Figure 5.** Variation in the steady-state friction coefficient ( $\mu_{ss}$ ) and steady-state porosity ( $V_{ss}$ ) of granular materials as function of velocity. (a, b) 0.2 mm glass beads at three normal-stress conditions. (c, d) 1 mm quartz sand at three normal-stress conditions (results using the ICL apparatus).

state friction coefficients seemed to merge to the same value under the same shear velocity, as shown in Figures S8a–S8d of the Supporting Information S1. From 0.5 to 0.01 m/s, the steady-state friction coefficients for different particle size were quite different even under the same shear speed, as shown in Figures S8e–S8h of the Supporting Information S1.

The mechanical data of the low-to-high rotary-shear apparatus (LHVR) on crushable quartz sand and fluorspar particles are presented in Figures 8a and 8b with different shear velocities from 0.0001 to 2 m/s. Extensive weakening was observed for both materials under comparatively higher velocity (above about 1 m/s). Extensive crushing was observed after tests on both materials (Hu et al., 2022).

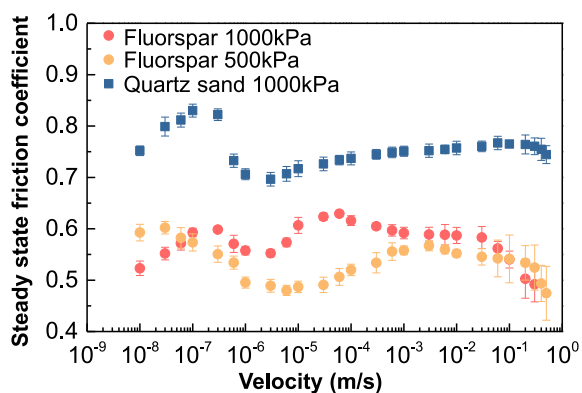
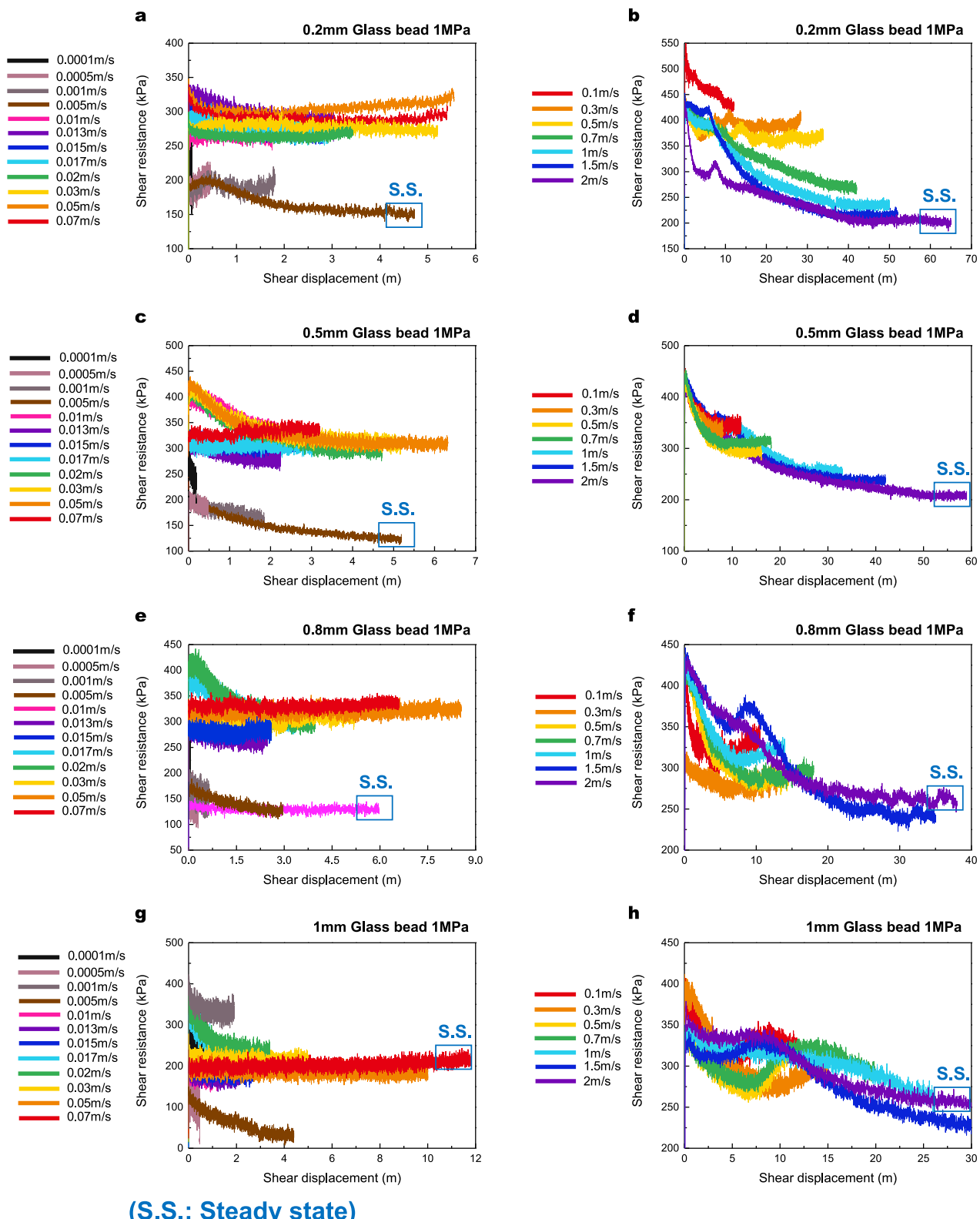


**Figure 6.** Variation in the steady state friction coefficient as functions of velocity for quartz sand at 1,000 kPa and fluorspar at 500 and 1,000 kPa (results from the ICL apparatus).

The relationships between  $\mu_{ss}$  (steady-state friction coefficient) and velocity for the four different grain diameters of glass beads were analyzed. The overall variation was that  $\mu_{ss}$  first decreased with increasing velocity; it then started to increase when velocity was about 0.01 m/s; when velocity exceeded 0.1 m/s,  $\mu_{ss}$  decreased again with increasing velocity (as shown in Figure 9a). The  $\mu_{ss}$  value decreased with increasing grain diameter under the same conditions. For different granular materials, the  $\mu_{ss}$  of quartz sand was greater than that of fluorspar, and the  $\mu_{ss}$  of glass beads was the smallest at lower velocities. All of three kinds of granular materials exhibited a pattern of  $\mu_{ss}$  decreasing, increasing, and then decreasing sharply to about 0.2 with increasing velocity (as shown in Figure 9b), which was unrelated to the particle size or to the grain type (whether it was broken or not). The variation pattern of  $\mu_{ss}$  with velocity for glass beads (Figure 9c) and quartz sand (Figure 9d) were also similar for different normal stress conditions. The detailed mechanical results of 0.2 mm glass beads at 500 kPa and 1 mm quartz sand at 200 kPa are shown in Figures S9 and S10 of the Supporting Information S1 respectively.



(S.S.: Steady state)

**Figure 7.** Mechanical results for each velocity at using glass beads with of different sizes under 1,000 kPa on the LHVR apparatus.

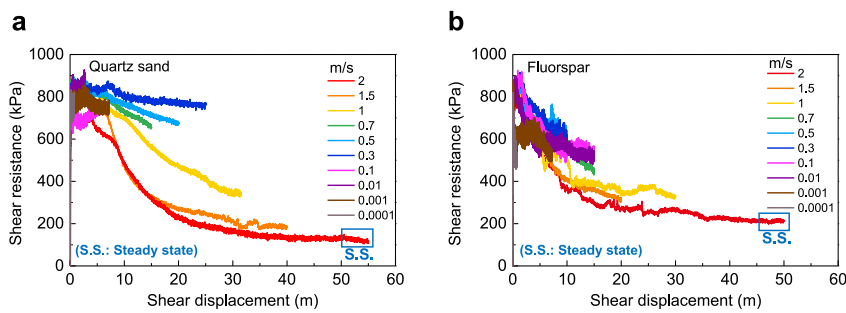


**Figure 8.** The mechanical data of the high-velocity rotary tests (LHVR) on crushable mineral particles (quartz sand and fluorspar). (a) The mechanical data of high-speed rotary tests on quartz sand at 1,000 kPa. (b) The mechanical data of high-speed rotary tests on fluorspar at 1,000 kPa.

### 3.2.2. Acoustic Data Analysis

We monitored acoustic signals for each experiment. We used five representative experiments of glass beads with a size of 1 mm under a normal stress of 1,000 kPa and with different shear velocities (representatively 0.001, 0.1, 0.5, 1, and 2 m/s) to analyze changes in the mode of interaction between grains as velocity increased. Figures 10a, 10e, 10i, 10m, and 10q shows the results of mechanical data at each shear velocity. As velocity increased, the friction coefficient of glass bead packs gradually weakened and a higher acoustic amplitude was recorded during shearing (Figures 10b, 10f, 10j, 10n, and 10r). The acoustic energy was calculated based on the monitoring of the AE signal using the equation:

$$E_a = A_v^2 \quad (8)$$

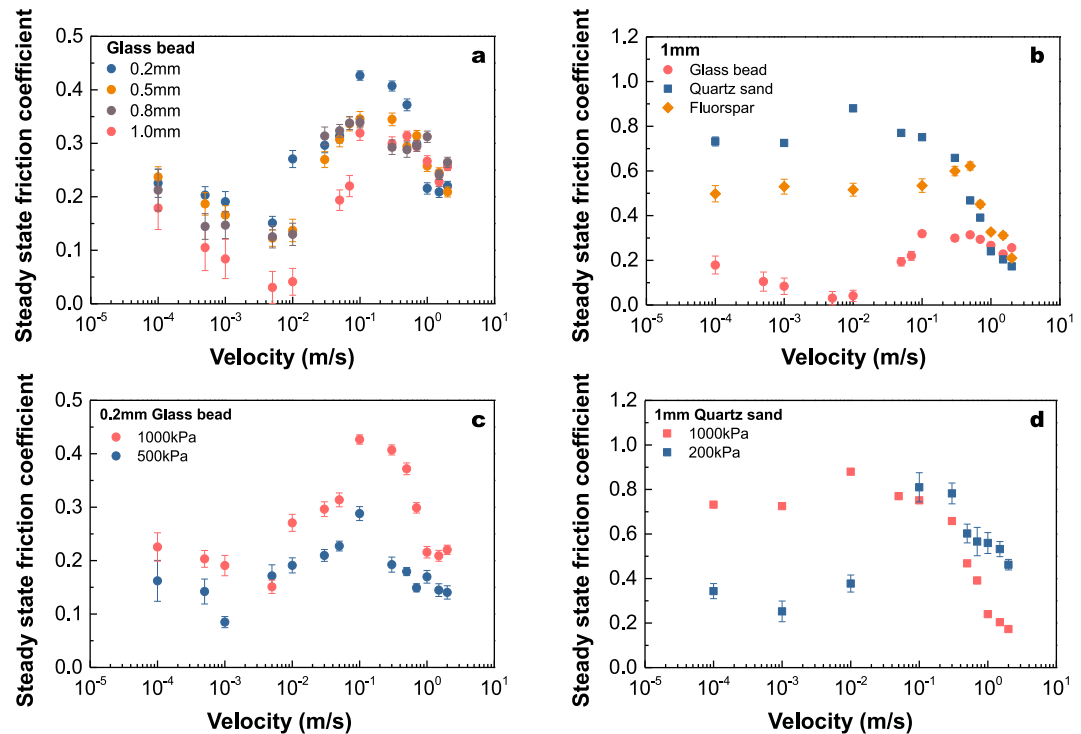


**Figure 9.** Variation of the  $\mu_{ss}$  (steady-state friction coefficient) of granular materials as a function of shear velocity for the LHVR tests. (a)  $\mu_{ss}$  analysis for glass beads of four different sizes (0.2, 0.5, 0.8, and 1.0 mm) with different shear velocities at a normal stress of 1,000 kPa. (b)  $\mu_{ss}$  for three granular materials with a size of 1 mm with different velocities (glass beads, quartz sand and fluorspar) at a normal stress of 1,000 kPa. (c) Variation of  $\mu_{ss}$  of 0.2 mm glass beads as a function of velocity at 500 and 1,000 kPa. (d) Variation of  $\mu_{ss}$  of 1 mm quartz sand as a function of velocity at 200 and 1,000 kPa.

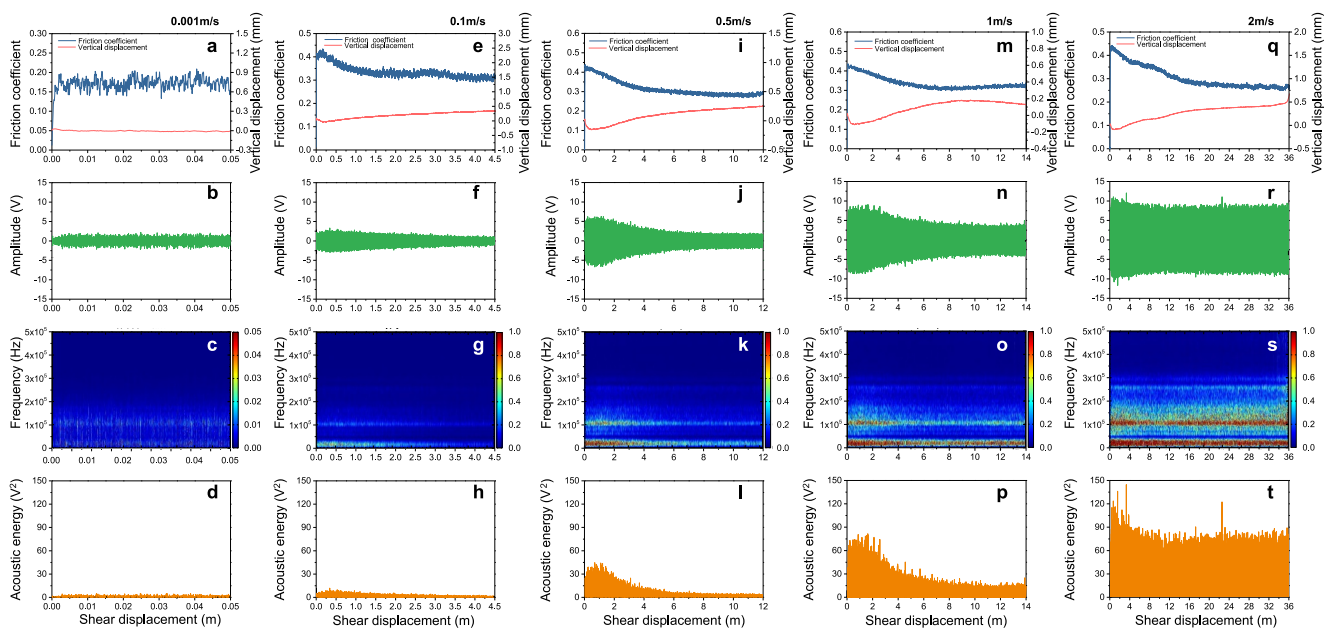


**Figure 10.** Acoustic emissions at different shear velocities of 1 mm glass beads on the LHVR apparatus. (a, e, i, m, q) Relationship between friction coefficient, vertical displacement and shear displacement for the five velocity conditions from low to high. (b, f, j, n, r) Relationship between acoustic amplitude and shear displacement. (c, g, k, o, s) Relationship between acoustic frequency and shear displacement. (d, h, l, p, t) Relationship between acoustic energy and shear displacement.

where  $A_v$  is the AE amplitude measured in volts. The acoustic energy that can reflect the granular temperature (Taylor & Brodsky, 2017) also increased with increased velocity, as shown in Figures 10d, 10h, 10l, 10p, and 10t.

We used the short-term Fourier transform method (Allen, 1977) to analyze the acoustic waveforms generated by shearing at different velocities. The AE frequency was found to be lower at slower velocities, and only two bands of a few tens of kHz and about 100 kHz were visible. We noted the AE signal of the apparatus before the experiment. The results showed that the noise signal (Figure S13 in Supporting Information S1) was stable and the intensity was much smaller than the AE signal generated by the movement of the sample. As the shear velocity increased, more acoustic emissions appeared in the 200 and 300 kHz bands. The acoustic amplitude increased with increasing shear velocity, as shown in Figures 10b, 10f, 10j, 10n, and 10r. The variation of acoustic energy with velocity showed the same pattern of amplitude (Figures 10d, 10h, 10l, 10p, and 10t). The acoustic emission band generated during shearing showed a stepwise increase with increasing velocity.

Under different grain diameter condition, acoustic energy increased with increasing inertia number ( $I$ ). At about  $I = 10^{-3}$ , the growth trend of acoustic energy started to steepen (Figure 11a). The shear velocity at this point was about 0.1 m/s and the  $\mu_{ss}$  started to weaken (Figure 11a). We normalized acoustic energy by grain mass and found

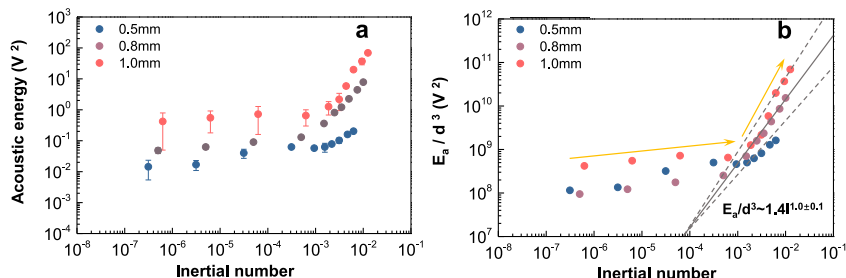


**Figure 11.** (a) The relationship between acoustic energy ( $E_a$ ) and inertial number ( $I$ ) for three grain diameters of glass beads. (b) Acoustic energy normalized by grain mass, that is, grain diameter cubed ( $E_a/d^3$ ) as a function of inertial number ( $I$ ).

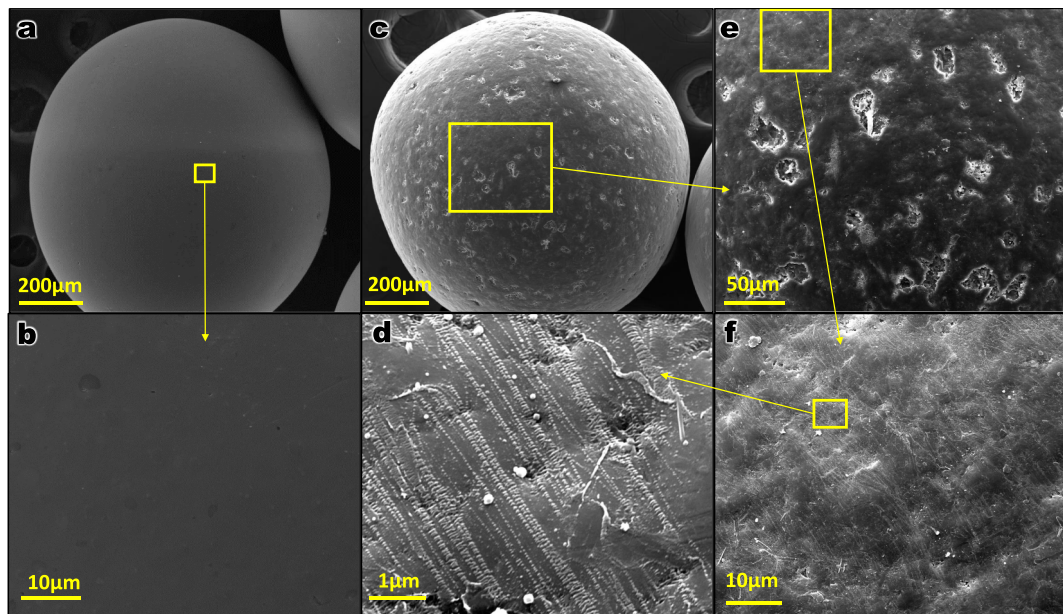


**Figure 12.** SEM images of one of the original 1 mm glass bead and one of a 1 mm glass bead after 1,000 kPa at 2 m/s experiment at LHVR. (a, b) Image of an original glass bead at increasing magnifications. (c–f) Images of a glass bead after tests at increasing magnifications as indicated.

that these relationships approached each other for all grain sizes (Figure 11b). The results showed a two-stage increase in granular temperature with increasing  $I$ , from gentle to steep. After the high-velocity weakening phase was entered, the data were averaged across all three grain diameter ranges, and the relationship observed was:

$$E_a/d^3 \cong 1.4 I^{1.0 \pm 0.1} \quad (9)$$

Taylor and Brodsky (2017) obtained a similar relationship under low normal stress:

$$E_a/d^3 \cong I^{1.0 \pm 0.1} \quad (10)$$

The results of acoustic monitoring using the ICL apparatus are shown in Figures S9 and S10 of the Supporting Information S1.

### 3.3. Grain-Surface Textures

#### 3.3.1. SEM Observations

The grain-surface textures revealed the evidence of interactions between particles. We examined SEM images of one representative 1 mm glass bead before test and after a high shear-velocity experiment under a normal stress of 1,000 kPa and shear velocity of 2 m/s. The surface of an original glass bead was relatively smooth (Figures 12a and 12b), while the surface of a bead after shearing was pitted. The surface texture after the high shear-velocity experiment had two main features. The surface was scattered with sharply defined pits that looked like those left by violent collisions of particles (Figure 12c) and these pits had a diameter of approximately 20  $\mu\text{m}$  (Figure 12e). These impact pits might be due to the increase in velocity, as the shear granular flow became “gas-like” flow, and the interaction between the particles changed from friction-driven to collision-driven (Bagnold, 1954; Campbell, 2005; Jaeger et al., 1996). Although the surface between the sharp pits appears relatively smooth, it is covered with streaks. At higher magnification, the grain surface appeared to be covered with relatively long, sub-parallel curvilinear traces (Figures 12d and 12f). We suspect that these traces might be “chatter marks” of stick-slip formed by particle friction in a high-frequency vibration field during high-velocity shearing or slip of one

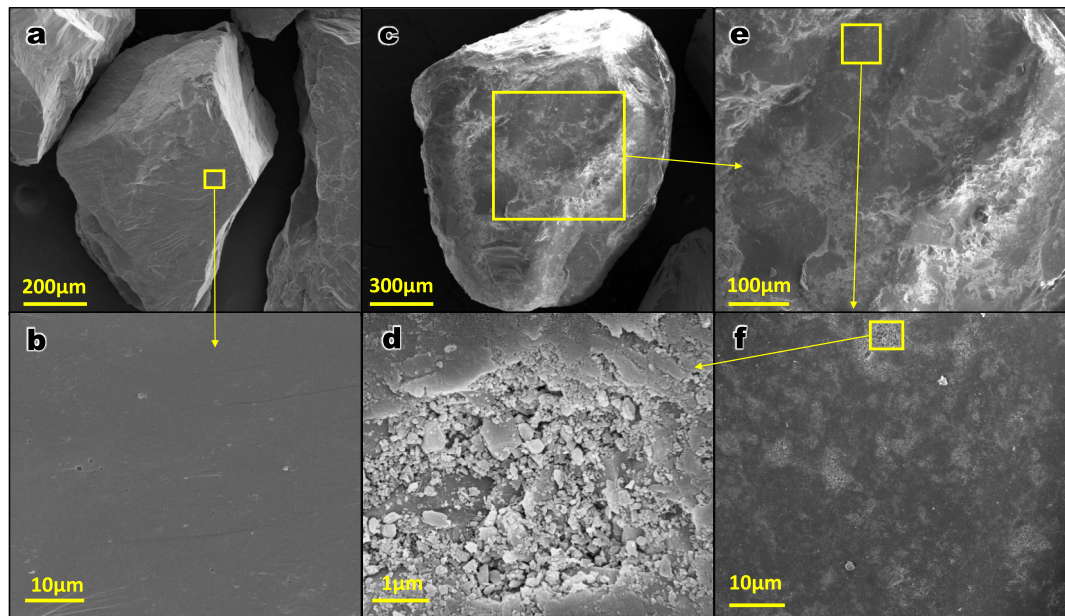


**Figure 13.** SEM images of one of the original 1 mm quartz sand particles and one of the 1 mm quartz sand particles after the 1,000 kPa at 2 m/s experiment at LHVR. (a, b) Image of an original quartz sand particle at increasing magnifications. (c–f) Images of a quartz sand grain after the test, at increasing magnifications.

particle past another. We selected large particles in the quartz sand samples after high-velocity shearing for SEM observation as well. The micromorphology of 1 mm quartz sand before the test and after a high shear-velocity experiment under a normal stress of 1,000 kPa and shear velocity of 2 m/s is shown in Figure 13. Although no serried “chatter marks” were similar to those discovered on the surface of glass beads after the test, pits that may be caused by grain collision were also present on the surface of quartz sand, as shown in Figures 13c–13f. The size of pits on the surface of quartz sand is smaller than that on the surface of glass beads, and were only 6–10  $\mu\text{m}$ .

### 3.3.2. Confocal Microscope Observations

The SEM images did not show the topography of the particle surface, so we used a Confocal Microscope (CM) to further analyze the surface roughness of the original glass beads and the glass beads after shearing at 1,000 kPa at 2 m/s at LHVR (Figures 14a and 14d). We selected the core area of the CM images (yellow line area in Figures 14a and 14d) and removed the sphere shape with a diameter of 1 mm (Figures 14b and 14e). We used  $S_a$  to denote the roughness of the area shape, which represents the arithmetic mean deviation of the area shape (David, 2004), defined as:

$$S_a = (1/NM) \sum_{i=1}^N \sum_{j=1}^M |Z_{ij}| \quad (11)$$

In this context,  $Z$  refers to the distance between a point on the contour of the object surface area and a reference plane. Meanwhile,  $M$  and  $N$  represent the number of sampling points in two perpendicular directions within the evaluation area. The surface roughness  $S_a = 0.1040$  is for the original glass beads and  $S_a = 0.3927$  for the glass beads after shearing at 1,000 kPa in the 2 m/s experiment (Figures 14c and 14f). The rapid shearing had increased the surface roughness of the glass beads.

## 4. Experimental Data Interpretation and Extrapolation of $\mu$ - $v$ Model

We examined how  $\mu_{ss}$  for three kinds of granular materials including quartz sand, fluorspar, and glass beads decreased, increased, and then decreased with velocity in the range of  $10^{-8}$ –2 m/s using the ICL and LHVR apparatus. The modified ICL results and the LHVR results were stitched together under the same experimental

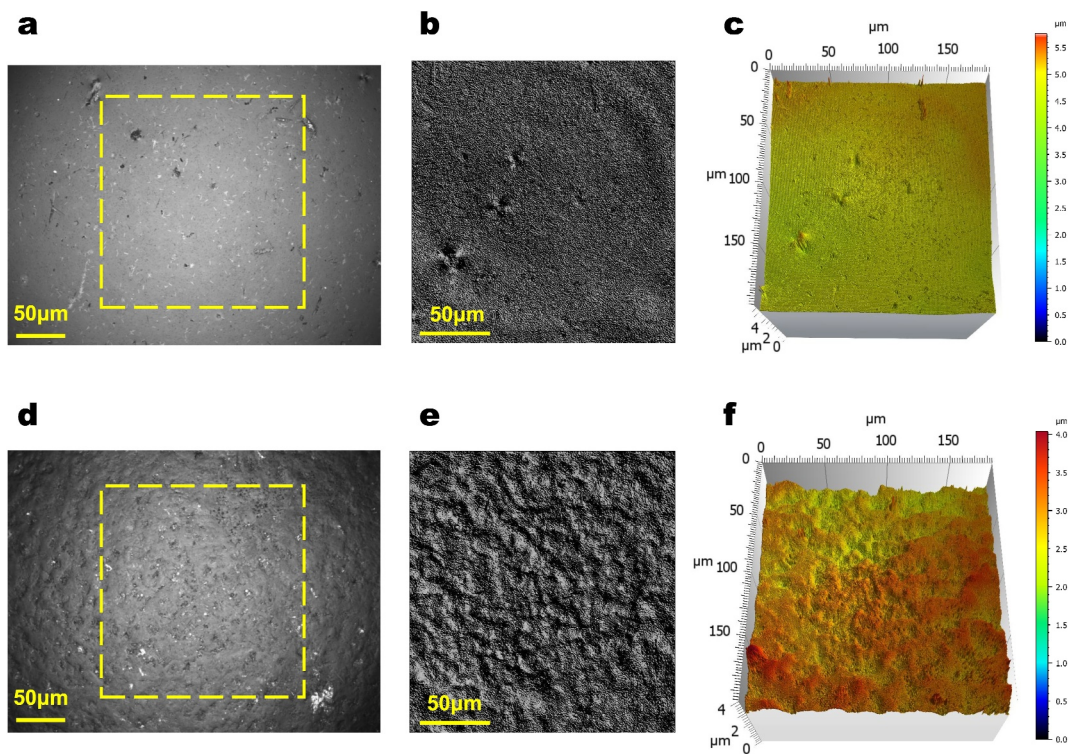


**Figure 14.** 3-D morphology representative results of one of the original 1 mm glass beads and one after a high shear-velocity experiment at 1,000 kPa at 2 m/s at LHVR. (a) Confocal microscope (CM) image of an original glass bead. (b, c) The 3D morphology results after removing the shape of the yellow line area in (a). (d) CM image of a glass bead after the test. (e, f) The 3D morphology results after removing the shape of the yellow line area in (b).

conditions, as shown in Figure 15. Figure 15 showed the velocity-dependent results for glass beads, quartz sand and fluorspar over the full range of shear velocities tested. They represented two different granular materials (round and angular, crushed or not), and the common law can represent a more general result for granular materials. Across the tested velocity range,  $\mu_{ss}$  exhibited two strengthening regimes and two weakening regimes, in a very broad “m-like” shape, as shown in Figure 16b. These four regimes are discussed separately below.

## 5. Discussion

This study employed the ring shear mode, using as few instruments as possible (only the ICL ring shear apparatus and LHVF high-velocity friction machine), and achieved the clearest and most comprehensive “M-shape” conclusion to date. Previous studies used at least three different instruments for their experiments, including biaxial, triaxial, torsional shear, and high-speed friction machines. A limitation is that these instruments had different shear modes, leading to substantial differences in friction within overlapping velocity intervals. The diverse shear modes made it challenging for researchers to believe in the “M-shape” conclusion. We discovered frictional rate-dependent effects of granular materials (including crushed and uncrushed materials) across nine orders of magnitude from  $10^{-8}$  to 2 m/s. In this way, four regimes of granular material mechanical behavior as a function of shear velocity were clearly delineated. The low-speed experiments in the Di Toro et al. (2011) and were the result of rock friction, which could not reflect the friction characteristics. Previous studies just spliced frictional velocity effect of different rocks and a few gouges in a small velocity range (less than 5 orders of magnitude), so, it is also not possible to obtain the other three regimes clearly except the high-speed weakening regime. We discovered that

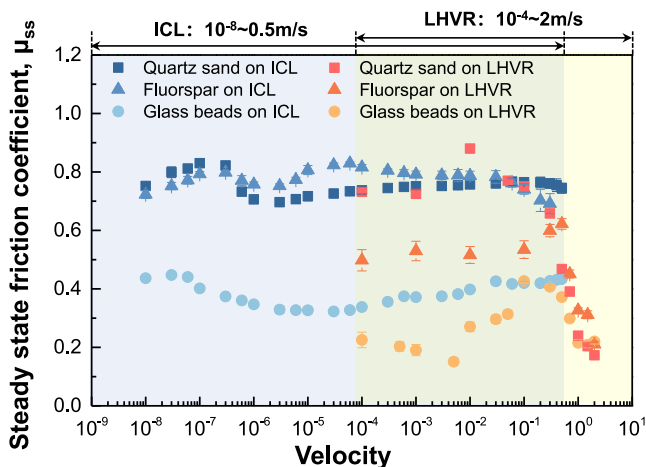


**Figure 15.** Test results conclusions and  $\mu$ - $v$  model. The ICL and LHVR results were combined to show the three kinds of granular materials of quartz sand, fluorspar, and glass beads at 1,000 kPa.

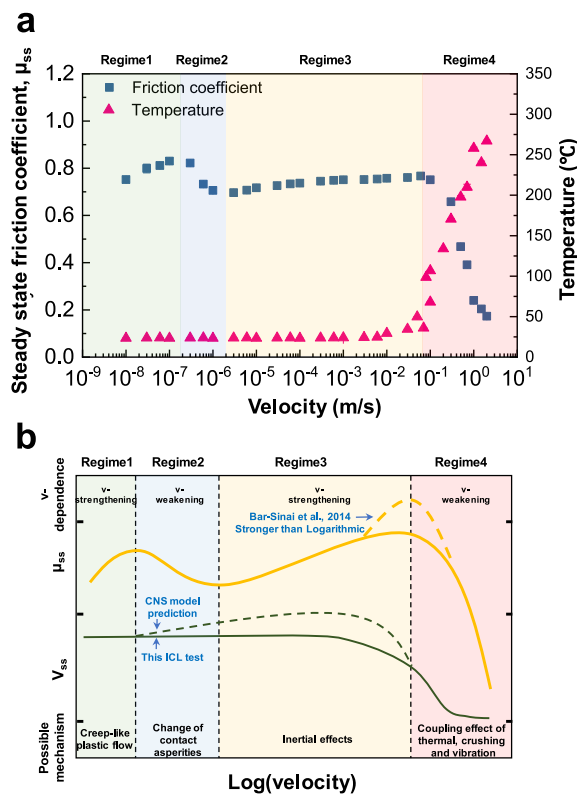


**Figure 16.** Test results conclusions and  $\mu$ - $v$  model. (a) Results of steady-state friction coefficient and temperature with shear velocity of 1 mm quartz sand at 1,000 kPa. (b)  $\mu$ - $v$  model and volume variation over the full range of laboratory shear velocities.

the weakening regime existed not only in broken materials but also in unbroken granular materials under shear velocity ( $v > 0.1$  m/s) and normal stress ( $>0.2$  MPa). In the previous studies of granular physics, rate-dependent study of unbroken granular material is also an important topic. However, the previous study is mostly based on very low normal stress (tens of Pascals), the mechanical behavior of unbroken granular flow under comparatively high normal stress is not clear. Bagnold (1954), Jaeger et al. (1996), Campbell (2005), and Jop et al. (2006) concluded that granular flow had a quasi-static regime, transitional regime and inertial regime. At high shear velocities granular flow would go to the gas state and the friction would increase continuously or remained smooth due to inertia under low normal stress (tens of Pascals). The weakening regime of unbroken granular flow was not discovered in the previous studies. This study discovered that the weakening regime exists in unbroken granular materials (glass beads), which was not only a potential contribution to earth science, but also equally important for granular physics.

We compiled a number of references to analyze the physical mechanisms of each regime of the  $\mu$ - $v$  model. Possible velocity-strengthening or weakening mechanisms are listed in Table 2.

### 5.1. Mechanisms of the Quasi-Static Regime

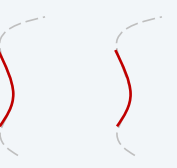
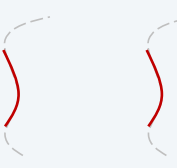
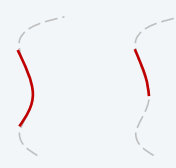
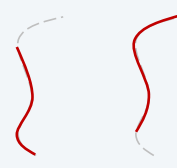
First,  $\mu_{ss}$  exhibited strengthening at very slow shear velocities (Regime 1 in Figure 16b). Jaeger et al. (1996) and Campbell (2005) described the very slow shear of granular materials as “solid-like” granular flow, and called this regime the “quasi-static regime (or critical regime).” Many studies on quartz gouge that have demonstrated slip can be unstable at very low shear velocities ( $10^{-8}$ – $10^{-7}$  m/s), with the stability being largely controlled by the effective normal stress, gouge grain size and stiffness of the loading system (Bedford & Faulkner, 2021; Gu & Wong, 1994; Scuderi et al., 2017). The results from our ICL experiments indicated shear resistance strengthening in this regime.

Shimamoto (1986) and Kuwano and Hatano (2011) found similar experimental results with halite (rock salt) in a triaxial apparatus and granite in a rheometer. Material like halite falls in the flow regime at a very low slip rate and the shear resistance depends on shear velocity (Shimamoto, 1986). Estrin and Bréchet (1996) highlighted the similar shear strengthening behavior of both ductile and brittle materials. As the shearing process of granular materials is irreversible, we believed that shear strengthening at very slow velocities was due to a creep-like plastic flow response (Chen et al., 2017; Estrin & Bréchet, 1996; Niemeijer & Spiers, 2007; Shimamoto, 1986). The ICL ring shear apparatus controlled the extremely slow experiments through the control of the average shearing velocity (if we zoom in on the relationship between shear resistance and shear displacement, we notice a step-like change in shear resistance before reaching a steady state, shown as Figure S14 in Supporting Information S1). The limitations of replacing instantaneous velocity with average velocity under extremely low-velocity conditions in this study meant that the experimental results at very low velocities were provided for reference only. Furthermore, we tried a new experimental method to verify that if the shear displacement of about 1 mm after a 29.4-hr shearing period enable the shear to reach the steady state. First, we sheared the sample to a steady state at a velocity of  $10^{-5}$  m/s, and then immediately reduced the shear velocity to  $10^{-8}$  m/s, so that the extremely slow experiment was completed under steady state condition, shown in Figure S15 of the Supporting Information S1. The shear resistance obtained was basically consistent with the resistance of extremely slow shear in the Result part. Description in this study 29.4-hr shearing period enable the shear to reach the steady state.

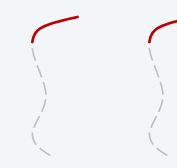
### 5.2. Mechanisms of the Transitional Regime

At slightly increased shear velocities ( $10^{-7}$ – $10^{-5}$  m/s),  $\mu_{ss}$  exhibited the first weakening (Regime 2 in Figure 16b). After the creep regime, Reinen et al. (1992), Chester and Higgs (1992), Putelat et al. (2007), and Noda and Shimamoto (2010) discovered similar experimental velocity-weakening phenomenon using serpentinite, quartz gouge, spring-block, halite. They called this regime the “transitional regime” and thought that this

**Table 2**  
*Possible Mechanisms of the  $\mu\text{-}\nu$  Model*

Reference	Model	Material	Mechanism
Shimamoto (1986), Reinen et al. (1992), Chester and Higgs (1992), Estrin and Bréchet (1996), Putelat et al. (2007), and Noda and Shimamoto (2010)		Both ductile and brittle material; Halite; Granular material; Serpentinite; Quartz gouge; Spring-block	Creep-like plastic/ductile flow → Flow-to friction-governed rheology
Jaeger et al. (1990) and Léopoldès et al. (2020)		Both ductile and brittle material; Granular material	Unstable intermittent flow/slippage(stick-slip) → Inertial
Scholz and Engelder (1976), Dieterich (1979), Tullis and Weeks (1986), Kilgore et al. (1993), Heslot et al. (1994), Baumberger et al. (1999), Rice et al. (2001), Baumberger and Caroli (2006), and Bar-Sinai et al. (2014)		Bristol Board; Polymer Glass; Rock	“Rejuvenation” of contact asperity → Thermally activated rheology
Lu et al. (2007) and Elst et al. (2012)		Glass beads; Angular beach sand and spherical foundry sand	Internal vibration → Inertial
Bagnold (1954), Savage (1984), Jaeger et al. (1996), Iverson (1997), Clement (1999), Weeks (1993), GDRMiDi (2004), da Cruz et al. (2005), Campbell (2006), Iop et al. (2006), Hatano (2007), Koval et al. (2009), Kuwano and Hatano (2011), and Kuwano et al. (2013)		Granular Material; Rock or analog materials	Inertial
Sleep (1995), Niemeijer and Spiers (2007), den Hartog and Spiers (2014), Chen and Spiers (2016), and Chen et al. (2017)		Granular material; Fault gouge	Creep-like plastic flow → Dilatation of effective shear zone → Grain boundary sliding
Aharonov and Scholz (2018)		Quartz; Granite	Rate and state theory → Thermally activated rheology → “Flash” heating/melting at asperity contacts
Brune et al. (1990), Castro et al. (1991), Anoshehpoor and Brune (1994), and Brune and Thatcher (2002)		Foam rubber blocks	Normal stress reduction or loss of contact from normal interface vibrations
Weertman (1963, 1980), Harris and Day (1997, 2005), Xia et al. (2005), Andrews and Harris (2005, 2006), and Rudnicki and Rice (2006)		Two materials having different elastic properties or different permeability	Dynamic normal stress reduction from elastic or permeability mismatch

**Table 2**  
*Continued*

Reference	Model	Material	Mechanism
Melosh (1979), Melosh and Girdner (1995), Melosh (1996), Melosh and Ivanov (1999), Collins and Melosh (2002), and Hu et al. (2022)		Granular Material	Acoustic Fluidization
Lachenbruch (1980), Mase and Smith (1985), Lee and Delaney (1987), Goldsby and Tullis (1997), Andrews (2002), Rempel and Rice (2006), Rice (2006), Rice and Cocco (2007), and Hu et al. (2019)		Rock and analog materials	Thermal pressurization of pore fluid
Bowden and Ridler (1936), Blok (1937), Jaeger (1942), Archard (1958), Bowden and Persson (1960), Etiles (1986), Lim and Ashby (1987), Lim et al. (1989), Molinari et al. (1999), Rice (1999, 2006), Beeler and Tullis (2003), Beeler et al. (2008), De Paola et al. (2011), and Tisato et al. (2012)		Rock and analog materials; Fault gouge	“Flash” heating/melting at asperity contacts
Philpot (1964), McKenzie and Brune (1972), Sibson (1975), Wenk (1978), Maddock (1986), Mase and Smith (1987), Swanson (1988), Magloughlin and Spray (1992), Kanamori and Heaton (2000), Bjornenud and Magloughlin (2004), Di Toro and Pennachioni (2004), Ferre et al. (2005), Fialko and Khazan (2005), Hirose and Shimamoto (2005), and Rempel and Rice (2006) Goldsby and Tullis (1998, 2002), Titone et al. (2001), and Di Toro et al. (2004)		Rock and analog materials; Fault gouge	Interfacial lubrication by friction melt
De Paola et al. (2015), Green et al. (2015), and Chen et al. (2020)		Carbonate rock; Calcite	Superplastic flow
Han et al. (2007), Reches and Lockner (2010), and Chen et al. (2013)		Rock and analog materials; Fault gouge	Nanopowder lubrication
McSaveney and Davies (2007) and Hu et al. (2020)		Granular Material	Inertial → Grain crushing

velocity-weakening was due to flow- to friction-governed rheology. Some studies used granular material to propose that unstable intermittent flow (stick-slip) may cause the velocity-weakening because stick-slip behavior was obvious in this regime (Estrin & Bréchet, 1996; Jaeger et al., 1990; Léopoldès et al., 2020). Sleep (1995), Niemeijer and Spiers (2007), den Hartog and Spiers (2014), and Chen et al. (2017) suggested that the dilation of the granular effective shear zone caused this weakening, but it was too difficult to monitor the volume change of the effective shear zone. Our experimental results from ICL showed no significant volume dilation of the whole sample in this regime for either glass beads or quartz sand (Figures 5b, 5d, and 16b). Based on rate- and state-dependent friction laws, some studies used polymer glass and rocks to propose that on the particle surfaces the “lifetime” of a contact asperity was shorter at higher shear velocity, that is, “rejuvenation,” thus higher velocity corresponded to lower friction (Bar-Sinai et al., 2014; Baumberger & Caroli, 2006; Baumberger et al., 1999; Kilgore et al., 1993; Tullis & Weeks, 1986). Lu et al. (2007) and Elst et al. (2012) proposed the idea of “auto-acoustic compaction” using acoustic emissions and externally applied vibration and suggested that the weakening in this regime was caused by internal acoustic vibrations in the shear particle system. In this study, we did not have solid evidence to reveal the physical mechanisms of velocity-weakening in Regime 2. Based on previous studies, we hypothesized that the velocity-weakening of granular materials in the transitional regime fundamentally was due to changes in contact asperities, which can be caused by stick-slip, dilation of the granular effective shear zone, and internal vibration. As to which of these three factors dominates the changes in asperity, further research is needed.

### 5.3. Mechanisms of the Inertial Regime

As the shear velocity increased further, the contact area is small enough to reach a critical value at a certain shear velocity (Bar-Sinai et al., 2014) and the sample begins to compact and the friction begins to increase. Thus, the v-strengthening phenomenon in Regime 3 may be attributed to compaction of the slip zone enhanced (Aharonov & Scholz, 2018; Bar-Sinai et al., 2014; Baumberger & Caroli, 2006; Baumberger et al., 1999; Heslot et al., 1994; Rice et al., 2001). Our experimental sample volume from ICL also began to compact in this regime. On the other hand, Chen et al. (2017) suggested that the dilatant effect becomes less important and the shear strength was controlled by grain boundary sliding, which was inherently velocity strengthening.

Bar-Sinai et al. (2014) deduced that there was a stronger than logarithmic regime within this regime but we did not find any similar phenomenon from our experimental results (Figures 15 and 16b). For granular materials, as the shear velocity increases, the inertia of the particles cannot be ignored. The Regime 3 in Figure 16b was called the “inertial regime,” which was relatively well understood from many studies (Bagnold, 1954; Campbell, 2006; Clement, 1999; da Cruz et al., 2005; GDRMiDi, 2004; Hatano, 2007; Iverson, 1997; Jaeger et al., 1996; Jop et al., 2006; Koval et al., 2009; Kuwano & Hatano, 2011; Kuwano et al., 2013; Savage, 1984; Weeks, 1993). At shear velocities above a certain level, the shearing granular material exhibited a fluid-like, inertial flow regime. Shear and normal stresses were then related to a particle momentum transfer rate (Bagnold, 1954; Campbell, 2005). Thus, a dimensionless coefficient inertial number  $I$  was introduced, as shown in Equation 1 (GDRMiDi, 2004; Savage, 1984). As  $\frac{d}{\sqrt{P/\rho}}$  is the velocity relaxation time in granular matter (Hatano, 2009),  $I$  may be regarded as an index for the inertial effects inside the flow. Many studies showed  $\mu_{ss}$  as an increasing function of  $I$  (da Cruz et al., 2005; GDRMiDi, 2004; Hatano, 2007; Jop et al., 2006; Koval et al., 2009). It should be noted that the  $I$  calculated herein was small due to the high  $P$  value (1,000 kPa) in our study, which was two orders of magnitude larger than the  $P$  values studied by previous studies. Therefore, a modification to allow for the high normal stress may need to be made to the conventional calculation of  $I$ .

### 5.4. Mechanisms of the Rapid-Shear Weakening Regime

At high shear velocities,  $\mu_{ss}$  showed another significant weakening (Figure 16b), which had several possible mechanisms, and no consensus has been reached until now. In this regime, the thermal weakening due to frictional heating was believed to be inevitable (Tullis, 2007). As ambient temperature increased significantly during shearing, several hypotheses have been proposed as contributing to rapid-shear weakening: “Flash” heating/melting at asperity contacts (Aharonov & Scholz, 2018; Archard, 1958; Beeler & Tullis, 2003; Beeler et al., 2008; Blok, 1937; Bowden & Persson, 1960; Bowden & Ridler, 1936; De Paola et al., 2011; Ettles, 1986; Jaegar, 1942; Lim & Ashby, 1987; Lim et al., 1989; Molinari et al., 1999; Rice, 1999, 2006; Tisato et al., 2012), interfacial lubrication by friction melt (Bjornerud & Magloughlin, 2004; Di Toro & Pennacchioni, 2004; Ferre et al., 2005;

Fialko & Khazan, 2005; Hirose & Shimamoto, 2005; Kanamori & Heaton, 2000; Maddock, 1986; Magloughlin & Spray, 1992; Mase & Smith, 1987; McKenzie & Brune, 1972; Philpotts, 1964; Rempel & Rice, 2006; Sibson, 1975; Swanson, 1988; Wenk, 1978), thermal pressurization of pore fluid (Andrews, 2002; Goldsby & Tullis, 1997; Hu et al., 2019; Lachenbruch, 1980; Lee & Delaney, 1987; Mase & Smith, 1985; Rempel & Rice, 2006; Rice, 2006; Rice & Cocco, 2007), interfacial lubrication by thixotropic silica gel (Di Toro et al., 2004; Goldsby & Tullis, 1998, 2002; Titone et al., 2001), and superplastic flow (Chen et al., 2020; De Paola et al., 2015; Green et al., 2015). Except thermal effect, Brune et al. (1990), Castro et al. (1991), Anooshehpoor and Brune (1994), and Brune and Thatcher (2002) used foam rubber blocks to propose that velocity-weakening may be due to normal stress reduction or loss of contact from normal interface vibrations. If two layers of materials have different elastic properties or different permeabilities, the effect of dynamic normal stress reduction from elastic or permeability mismatch would become obvious (Andrews & Harris, 2005, 2006; Harris & Day, 1997, 2005; Rudnicki & Rice, 2006; Weertman, 1963, 1980; Xia et al., 2005). For granular materials, rapid shear can cause intense grain crushing and the degree of crushing increased with increasing speed, resulting in velocity-weakening in this regime (Hu et al., 2020; McSaveney & Davies, 2007). As a large number of nanoparticles can be produced during the crushing process, nano-powder lubrication is also considered possible for velocity-weakening (Chen et al., 2013; Han et al., 2007; Reches & Lockner, 2010). Moreover, another idea called acoustic fluidization suggested that both grain crushing and vibration would produce many elastic waves, which also can cause velocity-weakening under rapid shear (Collins & Melosh, 2002; Melosh, 1979, 1996; Melosh & Girdner, 1995; Melosh & Ivanov, 1999).

In this study, we monitored the steady-state temperature results of the samples for each velocity condition. We discovered that the steady-state temperature of the granular material increased steeply at Regime 4, and it was clear that shear heating was probably responsible for the majority of the weakening observed at high velocity (Figure 16a). The results on glass beads in Figure 15 showed that a granular material also entered the weakening regime without crushing at high shear velocities. The difference in  $\mu_{ss}$  between quartz sand and glass beads in the weakening regime perhaps may be an approximation of the contribution of crushing in this regime.

Furthermore, many researchers used granular temperature to define the fluctuation energy of individual grains within a flow, and considered it as a basis for a kinetic theory of granular flow (Haff, 1983; Jaeger et al., 1996). Taylor and Brodsky (2017) demonstrated that acoustic energy ( $E_a$ ) was approximately linearly related to granular temperature. Our experimental results showed an abrupt change in  $E_a$  when  $\mu_{ss}$  entered the weakening regime, as shown in Figure 11. The abrupt change in  $E_a$  represented an abrupt change in the granular temperature. This may indicate that the granular flow underwent a phase change at this point and entered a true gas-like flow regime, where stresses were supported through grain-grain or grain-boundary collisions, analogous to a kinetic gas model. In the SEM images of the surface of glass-beads after shearing at 1,000 kPa in the 2 m/s experiment, there were many small pits, perhaps left by collisions (Figures 12c and 12e). Between the sharp-edged pits, however, the surface was covered with streaks, as if former sharp pits had been smoothed. At higher magnification, the grain surface was crossed by many relatively long, sub-parallel curvilinear traces that generally ignored the surface topography, but locally curved around lumps and into hollows (Figures 12d, 12f, 13c, and 13f). The surface roughness became rougher (Figure 14). Particles with rougher surfaces should have greater frictional resistance to each other, so we suspect that collisions between particles at Regime 4 were beginning to become apparent. The hypothesis of “Acoustic fluidization” suggests that vibrations may contribute to the high-velocity weakening regime (Collins & Melosh, 2002; Hu et al., 2020, 2022; Melosh, 1996). Based on the microstructural and acoustic measurements, we were not sure whether the intense vibrations generated by particle collisions could lead to friction weakening in addition to the two major factors of friction heating and particle crushing, which requires more in-depth studies in the future.

### 5.5. Formula Description

The experimental model in our study differed from previous studies in that we replaced two rock columns by granular material as the initial state of the shear zone. Chen et al. (2020) established a hypothesis based on the formation of two regions of a shear band and a bulk layer after shearing of two rock columns, and they regarded the shear band as a granular flow. As the hypothesis in Chen et al. (2020) was similar to our granular shear experiments, we would follow the equations of the “Chen-Niemeijer-Spiers” model to describe regime 1–3 in Figure 15b and we hope to further explain the physical mechanism of regime 4. Then the  $\mu$ - $v$  model can be expressed as a piecewise function:

$$\mu_{ss} = \left\{ \frac{RT}{\Omega} \ln \left[ \frac{1}{\Pi} \frac{v(d^{sb})^m}{B_{pl} L_t f_{pl}(\varphi_0)} \right] + \frac{E_a}{\Omega} \right\} / \sigma, \quad \text{Regime 1} \quad (12)$$

where  $v$  is shear velocity;  $\sigma$  is normal stress;  $E_a$  is activation energy;  $R$ , the gas constant;  $T$ , absolute temperature (K);  $\Omega$ , activation volume; a preexponential factor  $B_{pl}$  is adopted for the shear component of contact creep;  $L_t$ , the total gouge layer thickness.  $\Pi$  is a dimensionless factor that unifies the deformation in both zones;  $d^{sb}$ , is the average grain size of a shear band;  $m$ , is a grain size sensitivity factor;  $f_{pl}(\varphi)$ , a porosity function accounting for changes in grain contact area;  $\varphi$  is porosity and  $\varphi_0$  is the minimum porosity.

$$\begin{cases} \tan \psi_{ss} = H \left[ \frac{L_t \lambda}{Hv} E_{pl}(T, d, \sigma) \right]^{1/(M+N)} \\ \tilde{\mu}_{ss} = \tilde{\mu}^* + a_{\tilde{\mu}} \ln \left( \frac{v}{v^*} \right) \\ \mu_{ss} = \frac{\tilde{\mu}_{ss} + \tan \psi_{ss}}{1 - \tilde{\mu}_{ss} \tan \psi_{ss}} \end{cases}, \quad \text{Regime 2 and 3} \quad (13)$$

where  $\psi_{ss}$  is average dilatancy angle at a steady state;  $H$  is a constant representing the geometric pattern of the grains;  $\lambda$  is the localization degree;  $E_{pl}$  is the temperature-compensated value of the apparent activation energy;  $d$  is grain size;  $M$  is the sensitivity of stress intensification to porosity;  $N$  is the sensitivity of dilatation angle to porosity;  $\tilde{\mu}_{ss}$  is the grain boundary friction coefficient at a steady state;  $\tilde{\mu}^*$  is the reference  $\tilde{\mu}$  value at a reference shear velocity  $v^*$ . The sensitivity parameter  $a_{\tilde{\mu}}$  is given as  $a_{\tilde{\mu}} = kT/\sigma_l \Omega$ , where  $k$  is the Boltzmann constant, and  $\sigma_l$  is the local stress supported by individual asperity contacts.

Our study is currently unable to provide an accurate formula description for Regimes 3 and 4, and we have included them as a subject for future study. For the inertial regime (Regime 3 in Figure 16b), Formula 13 did not consider particle inertia. However, for granular materials, inertial effects are inevitably present as the shear rate increases. In future studies, we hope to quantitatively distinguish between the velocity-strengthening rates of thermal activation and inertial effects after correcting the calculation method for the inertial number ( $I$ ) under high-pressure conditions. For a rapid-shear weakening regime (Regime 4 in Figure 16b), Chen et al. (2020) regarded the shear zone as a superplastic flow and had considered the thermal effect and the crushing behavior during the shear process:  $\mu_{ss} = f(v, \varphi, d, T)$ . In a future study, based on acoustic emissions and microstructural observations in this study, we hope to quantitatively analyze the contribution of intense vibration due to grain collision to velocity-weakening, to derive a function coupling heating, crushing and vibration:  $\mu_{ss} = f(v, \varphi, d, T, E)$ , where  $E$  is the vibration strength.

## 5.6. Limitation and Future Study

The maximum normal stress we applied in this study is 1 MPa, which is much lower than that of natural faults, and is only applicable to landslides and rock avalanches. We will continue to study the velocity effect of friction of granular materials under high normal stress conditions (several tens of MPa) to accommodate natural faults in the future, and we have developed the latest high-speed friction apparatus, with a maximum normal stress of up to 100 MPa and a maximum shear velocity of up to 30 m/s.

Compared to quartz sand and fluorspar, glass beads exhibited greater fluctuations in frictional strength in Figure 9. As to why the friction in the velocity range of  $10^{-4}$ – $10^{-2}$  m/s of glass beads decreases, the physical mechanism cannot be explained in this study yet. We only considered that the shear glass beads in the velocity range of  $10^{-4}$ – $10^{-2}$  m/s are still in a transitional regime, and we believed that the physical mechanism that generated the transitional regime had not been agreed upon by previous researchers, which needs to be investigated in more depth.

## 6. Conclusion

This study investigated shear-velocity dependent friction across various granular materials, including glass beads, quartz sand, and fluorspar, using the ICL and LHVR apparatuses. The study identified four distinct shear-

velocity-dependent frictional regimes: a quasi-static regime, transitional regime, inertial regime, and rapid-shear weakening regime. These regimes appeared universal across different normal stresses, grain diameters, and shapes. Acoustic emissions during granular flow revealed a continuous increase in frequency during rapid shear, and reached up to 300 kHz. At a shear velocity of 0.1 m/s, the steady-state temperature and acoustic energy increased steeply. We proposed that shear heating and crushing was probably responsible for the majority of the weakening observed at high velocity. Based on the microstructural and acoustic measurements, we were not sure whether the intense vibrations generated by particle collisions could also lead to friction weakening.

## Data Availability Statement

The data files used in this paper are available in Hu (2022).

### Acknowledgments

We are supported by the NSFC for Distinguished Young Scholars of China (42325703) and the National Basic Research Program of China: basic research fund (42090051). We want to thank Yao Lu from Institute of Geology, China Earthquake administration for his help with high-speed rotary tests.

### References

- Aharonov, E., & Scholz, C. H. (2018). A physics-based rock friction constitutive law: Steady state friction. *Journal of Geophysical Research: Solid Earth*, 123(2), 1591–1614. <https://doi.org/10.1002/2016JB013829>
- Allen, J. (1977). Short time spectral analysis, synthesis, and modification by discrete Fourier transform. *IEEE Transactions on Acoustics, Speech, and Signal Processing*, 25(3), 235–238. <https://doi.org/10.1109/TASSP.1977.1162950>
- Andrews, D. J. (2002). A fault constitutive relation accounting for thermal pressurization of pore fluid. *Journal of Geophysical Research*, 107(B12), 12. <https://doi.org/10.1029/2002jb001942>
- Andrews, D. J., & Harris, R. A. (2005). The wrinkle-like slip pulse is not important in earthquake dynamics. *Geophysical Research Letters*, 32(23), L23303. <https://doi.org/10.1029/2005GL023996>
- Andrews, D. J., & Harris, R. A. (2006). Reply to comment by Y. BenZion on ‘The wrinkle-like slip pulse is not important in earthquake dynamics’. *Geophysical Research Letters*, 33(6), L06311. <https://doi.org/10.1029/2006gl025743>
- Anooshehpoor, A., & Brune, J. N. (1994). Dynamics and frictional heat generation in a foam rubber model of earthquake stick-slip. In *USGS red book NEHRP open-file report 94-228, proceedings of workshop LXIII the mechanical involvement of fluids in faulting* (pp. 443–459).
- Archard, J. F. (1958). The temperature of rubbing surfaces. *Wear*, 2(6), 438–455. [https://doi.org/10.1016/0043-1648\(59\)90159-0](https://doi.org/10.1016/0043-1648(59)90159-0)
- Bagnold, R. A. (1954). Experiments on a gravity-free dispersion of large solid spheres in a Newtonian fluid under shear. *Proceedings of the Royal Society of London. Series A*, 225(1160), 49–63. <https://doi.org/10.2307/99440>
- Bar-Sinai, Y., Spatschek, R., Brener, E. A., & Bouchbinder, E. (2014). On the velocity-strengthening behavior of dry friction. *Journal of Geophysical Research: Solid Earth*, 119(3), 1738–1748. <https://doi.org/10.1002/2013JB010586>
- Baumberger, T., Berthoud, P., & Caroli, C. (1999). Physical analysis of the state- and rate-dependent friction law. II. Dynamic friction. *Physical Review B: Condensed Matter*, 60(6), 3928–3939. <https://doi.org/10.1103/PhysRevB.60.3928>
- Baumberger, T., & Caroli, C. (2006). Solid friction from stick-slip down to pinning and aging. *Advances in Physics*, 55(3–4), 279–348. <https://doi.org/10.1080/00018730600732186>
- Bedford, J. D., & Faulkner, D. R. (2021). The role of grain size and effective normal stress on localization and the frictional stability of simulated quartz gouge. *Geophysical Research Letters*, 48(7), e2020GL092023. <https://doi.org/10.1029/2020GL092023>
- Beeler, N., & Tullis, T. (2003). Constitutive relationships for fault strength due to flash-heating. In *2003 SCEC annual meeting proceedings and abstracts* (p. 66). Southern California Earthquake Center, Palm Springs.
- Beeler, N. M., Tullis, T. E., & Goldsby, D. L. (2008). Constitutive relationships and physical basis of fault strength due to flash heating. *Journal of Geophysical Research*, 113(B1), B01401. <https://doi.org/10.1029/2007JB004988>
- Bjørnerud, A., & Magloughlin, J. F. (2004). Pressure-related feedback processes in the generation of pseudotachylites. *Journal of Structural Geology*, 26(12), 2317–2323. <https://doi.org/10.1016/j.jsg.2002.08.001>
- Blok, H. (1937). Measurement of temperature flashes on gear teeth under extreme pressure conditions. In *Proceedings of the General discussion on lubrication and lubricants* (Vol. 2, pp. 14–20). Institute of Mechanical Engineers.
- Bocquet, L., Losert, W., Schalk, D., Lubensky, T. C., & Gollub, J. P. (2001). Granular shear flow dynamics and forces: Experiment and continuum theory. *Physical Review E*, 65(1), 011307. <https://doi.org/10.1103/PhysRevE.65.011307>
- Bowden, F. B., & Persson, P. A. (1960). Deformation heating and melting of solids in high speed friction. *Proceedings of the Royal Society of London. Series A*, 260, 433–458.
- Bowden, F. P., & Ridler, K. E. W. (1936). Physical properties of surfaces. Part III: The surface temperature of sliding metals; the temperature of lubricated surfaces. *Proceedings of the Royal Society of London. Series A*, 154, 640–656.
- Bowden, F. P., & Tabor, D. (1964). *The friction and lubrication of solids*. Oxford University Press.
- Bromhead, E. N. (1979). A simple ring shear apparatus. *Ground Engineering*, 12(5), 42–44. [https://doi.org/10.1016/0148-9062\(80\)90043-1](https://doi.org/10.1016/0148-9062(80)90043-1)
- Brune, J. N., Johnson, P. A., & Slater, C. (1990). Nucleation, predictability, and rupture mechanism in foam rubber models of earthquakes. *Journal of Himalayan Geology*, 1, 155–166.
- Brune, J. N., & Thatcher, W. (2002). Strength and energetics of active fault zones. *International Handbook of Earthquake and Engineering Seismology*, 81A, 569–588.
- Bureau, L., Baumberger, T., & Caroli, C. (2002). Rheological aging and rejuvenation in solid friction contacts. *European Physical Journal E: Soft Matter*, 8(3), 331–337. <https://doi.org/10.1140/epje/i2002-10017-1>
- Campbell, C. S. (2005). Stress-controlled elastic granular shear flows. *Journal of Fluid Mechanics*, 539(-1), 273–297. <https://doi.org/10.1017/S0022112005005616>
- Campbell, C. S. (2006). Granular material flows: An overview. *Powder Technology*, 162(3), 208–229. <https://doi.org/10.1016/j.powtec.2005.12.008>
- Castro, R. R., Anderson, J. G., & Brune, J. N. (1991). Origin of high P/S spectral ratios from the Guerrero accelerograph array. *Bulletin of the Seismological Society of America*, 81(6), 2268–2288.
- Chen, J., & Niemeijer, A. R. (2017). Seismogenic potential of a gouge-filled fault and the criterion for its slip stability: Constraints from a microphysical model. *Journal of Geophysical Research: Solid Earth*, 122(12), 9658–9688. <https://doi.org/10.1002/2017JB014228>

- Chen, J., Niemeijer, A. R., & Spiers, C. J. (2017). Microphysically derived expressions for rate-and-state friction parameters,  $a$ ,  $b$ , and  $D_c$ . *Journal of Geophysical Research: Solid Earth*, 122(12), 9627–9657. <https://doi.org/10.1002/2017JB014226>
- Chen, J., Niemeijer, A. R., & Spiers, C. J. (2020). Microphysical modeling of carbonate fault friction at slip rates spanning the full seismic cycle. *Journal of Geophysical Research: Solid Earth*, 126, e2020JB021024. <https://doi.org/10.1029/essoar.10504397.1>
- Chen, J., & Spiers, C. J. (2016). Rate and state frictional and healing behavior of carbonate fault gouge explained using microphysical model. *Journal of Geophysical Research: Solid Earth*, 121(12), 8642–8665. <https://doi.org/10.1002/2016JB013470>
- Chen, X., Madden, A. S., Bickmore, B. R., & Reches, Z. (2013). Dynamic weakening by nanoscale smoothing during high velocity fault slip. *Geology*, 41(7), 739–742. <https://doi.org/10.1130/g34169.1>
- Chester, F. M., & Higgs, N. G. (1992). Multimechanism friction constitutive model for ultrafine quartz gouge at hypocentral conditions. *Journal of Geophysical Research*, 97(B2), 1859–1870. <https://doi.org/10.1029/91jb02349>
- Clement, E. (1999). Rheology of granular media. *Current Opinion in Colloid & Interface Science*, 4, 294–299. [https://doi.org/10.1016/S1359-0294\(99\)90004-3](https://doi.org/10.1016/S1359-0294(99)90004-3)
- Collins, G. S., & Melosh, H. J. (2002). Target weakening and temporary fluidization in large impact events. In *Lunar & planetary science conference XXXIII*.
- da Cruz, F., Emam, S., Prochnow, M., Roux, J.-N., & Chevoir, F. (2005). Rheophysics of dense granular materials: Discrete simulation of plane shear flows. *Physical Review E*, 72(2), 021309. <https://doi.org/10.1103/PhysRevE.72.021309>
- David, W. (2004). Surfaces and their measurement.
- den Hartog, S., & Spiers, C. J. (2014). A microphysical model for fault gouge friction applied to subduction megathrusts. *Journal of Geophysical Research: Solid Earth*, 119(2), 1510–1529. <https://doi.org/10.1002/2013JB010580>
- De Paola, N., Hirose, T., Mitchell, T., Di Toro, G., Togo, T., & Shimamoto, T. (2011). Fault lubrication and earthquake propagation in thermally unstable rocks. *Geology*, 39(1), 35–38. <https://doi.org/10.1130/g31398.1>
- De Paola, N., Holdsworth, R. E., Viti, C., Collettini, C., & Bullock, R. (2015). Can grain size sensitive flow lubricate faults during the initial stages of earthquake propagation? *Earth and Planetary Science Letters*, 431, 48–58. <https://doi.org/10.1016/j.epsl.2015.09.002>
- Dieterich, J. H. (1978). Time-dependent friction and the mechanics of stick-slip. *Pure and Applied Geophysics*, 116(4–5), 790–806. <https://doi.org/10.1007/BF00876539>
- Dieterich, J. H. (1979). Modeling of rock friction: 1. Experimental results and constitutive equations. *Journal of Geophysical Research*, 84(B5), 2161–2168. <https://doi.org/10.1029/jb084ib05p02161>
- Dieterich, J. H., & Kilgore, B. D. (1994). Direct observation of frictional contacts: New insights for state-dependent properties. *Pure and Applied Geophysics*, 143(1–3), 283–302. <https://doi.org/10.1007/BF00874332>
- Di Toro, G., Goldsby, D. L., & Tullis, T. E. (2004). Friction falls towards zero in quartz rock as slip velocity approaches seismic rates. *Nature*, 427(6973), 436–439. <https://doi.org/10.1038/nature02249>
- Di Toro, G., Han, R., Hirose, T., De Paola, N., Nielsen, S., Mizoguchi, K., et al. (2011). Fault lubrication during earthquakes. *Nature*, 471(7339), 494–498. <https://doi.org/10.1038/nature09838>
- Di Toro, G., & Pennacchioni, G. (2004). Superheated friction-induced melts in zoned pseudotachylites within the Adamello tonalites (Italian Southern Alps). *Journal of Structural Geology*, 26(10), 1783–1801. <https://doi.org/10.1016/j.jsg.2004.03.001>
- Elst, N. J. V. D., Brodsky, E. E., Bas, P. Y. L., & Johnson, P. A. (2012). Auto-acoustic compaction in steady shear flows: Experimental evidence for suppression of shear dilatancy by internal acoustic vibration. *Journal of Geophysical Research*, 117, B09314. <https://doi.org/10.1029/2011jb008897>
- Estrin, Y., & Bréchet, Y. (1996). On a model of frictional sliding. *Pure and Applied Geophysics*, 147(4), 745–762. <https://doi.org/10.1007/BF01089700>
- Ettles, C. M. M. (1986). The thermal control of friction at high sliding speeds. *Journal of Tribology—Transactions of the ASME*, 108(1), 98–104. <https://doi.org/10.1115/1.3261151>
- Ferdowsi, B., Griffa, M., Guyer, R. A., Johnson, P. A., & Carmeliet, J. (2014). Effect of boundary vibration on the frictional behavior of a dense sheared granular layer. *Acta Mechanica*, 225(8), 2227–2237. <https://doi.org/10.1007/s00707-014-1136-y>
- Ferre, E. C., Allen, J. L., & Lin, A. M. (2005). Pseudotachylites and seismogenic friction: An introduction to current research. *Tectonophysics*, 402(1–4), 1–2. <https://doi.org/10.1016/j.tecto.2005.03.013>
- Forri, F., Di Toro, G., Hirose, T., Han, R., Noda, H., Shimamoto, T., et al. (2011). Low- to high-velocity frictional properties of the clay-rich gouges from the slipping zone of the 1963 Vajont slide, northern Italy. *Journal of Geophysical Research*, 116(B9), B09208. <https://doi.org/10.1029/2011JB008338>
- Fialko, Y., & Khazan, Y. (2005). Fusion by earthquake fault friction: Stick or slip? *Journal of Geophysical Research*, 110(B12), B12407. <https://doi.org/10.1029/2005JB003869>
- GDR MiDi. (2004). On dense granular flows. *The European Physical Journal E*, 14(4), 341–365. <https://doi.org/10.1140/epje/i2003-10153-0>
- Goldsby, D., & Tullis, T. E. (1998). Experimental observations of frictional weakening during large and rapid slip. *Eos Transactions*, 79, F610.
- Goldsby, D. L., & Tullis, T. E. (1997). Shear heating induced pressurization of pore fluid as a dynamic fault weakening mechanism. *Eos Transactions*, 78, 472.
- Goldsby, D. L., & Tullis, T. E. (2002). Low frictional strength of quartz rocks at subseismic slip rates. *Geophysical Research Letters*, 29(17), 1844. <https://doi.org/10.1029/2002GL015240>
- Green, H. W. I. I., Shi, F., Bozhilov, K., Xia, G., & Reches, Z. (2015). Phase transformation and nanometric flow cause extreme weakening during fault slip. *Nature Geoscience*, 8(6), 484–489. <https://doi.org/10.1038/ngeo2436>
- Gu, Y., & Wong, T. (1994). Development of shear localization in simulated quartz gouge: Effect of cumulative slip and gouge particle size. *PAGEOPH*, 143(1–3), 387–423. <https://doi.org/10.1007/BF00874336>
- Haff, P. K. (1983). Grain flow as a fluid-mechanical phenomenon. *Journal of Fluid Mechanics*, 134(1), 401. <https://doi.org/10.1017/s0022112083003419>
- Han, R., Shimamoto, T., Hirose, T., Ree, J. H., & Ando, J. (2007). Ultralow friction of carbonate faults caused by thermal decomposition. *Science*, 316(5826), 878–881. <https://doi.org/10.1126/science.1139763>
- Harris, R. A., & Day, S. M. (1997). Effects of a low-velocity zone on a dynamic rupture. *Bulletin of the Seismological Society of America*, 87(5), 1267–1280. <https://doi.org/10.1785/bssa0870051267>
- Harris, R. A., & Day, S. M. (2005). Material contrast does not predict earthquake rupture propagation direction. *Geophysical Research Letters*, 32(23), L23301. <https://doi.org/10.1029/2005gl023941>
- Hatano, T. (2007). Power-law friction in closely packed granular materials. *Physical Review E*, 75(6), 060–301. <https://doi.org/10.1103/PhysRevE.75.060301>
- Hatano, T. (2009). Scaling of the critical slip distance in granular layers. <https://doi.org/10.1029/2009gl039665>

- Heslot, F., Baumberger, T., Perrin, B., Caroli, B., & Caroli, C. (1994). Creep, stick-slip, and dry-friction dynamics: Experiments and a heuristic model. *Physical Review E*, 49(6), 4973–4988. <https://doi.org/10.1103/PhysRevE.49.4973>
- Hirose, T., & Shimamoto, T. (2005). Growth of molten zone as a mechanism of slip weakening of simulated faults in gabbro during frictional melting. *Journal of Geophysical Research*, 110(B5), B05202. <https://doi.org/10.1029/2004jb003207>
- Hu, W. (2022). Variation in granular frictional resistance across nine orders of magnitude in shear velocity [Dataset]. *Figshare*. <https://doi.org/10.6084/m9.figshare.20626812.v1>
- Hu, W., Chang, C. S., McSaveney, M., Huang, R., Xu, Q., Zheng, Y., & Yu, J. (2020). A weakening rheology of dry granular flows with extensive brittle grain damage in high-speed rotary shear experiments. *Geophysical Research Letters*, 47(11), e2020GL087621. <https://doi.org/10.1029/2020GL087763>
- Hu, W., Huang, R., McSaveney, M., Yao, L., Xu, Q., Feng, M., & Zhang, X. (2019). Superheated steam, hot CO<sub>2</sub> and dynamic recrystallization from frictional heat jointly lubricated a giant landslide: Field and experimental evidence. *Earth and Planetary Science Letters*, 510, 85–93. <https://doi.org/10.1016/j.epsl.2019.01.005>
- Hu, W., Xu, Q., McSaveney, M., Huang, R., Wang, Y., Chang, C. S., et al. (2022). The intrinsic mobility of very dense grain flows. *Earth and Planetary Science Letters*, 580, 117389. <https://doi.org/10.1016/j.epsl.2022.117389>
- Iverson, R. M. (1997). The physics of debris flows. *Reviews of Geophysics*, 35(3), 245–296. <https://doi.org/10.1029/97RG00426>
- Jaegar, J. C. (1942). Moving sources of heat and temperature at a sliding contact. *Journal and Proceedings of the Royal Society of New South Wales*, 76(3), 203–224. <https://doi.org/10.5962/p.360338>
- Jaeger, H. M., Liu, C. H., Nagel, S. R., & Witten, T. A. (1990). Friction in granular flows. *EPL (Europhysics Letters)*, 11(7), 619–624. <https://doi.org/10.1209/0295-5075/11/7/007>
- Jaeger, H. M., Nagel, S. R., & Behringer, R. P. (1996). Granular solids, liquids, and gases. *Reviews of Modern Physics*, 68(4), 1259–1273. <https://doi.org/10.1103/RevModPhys.68.1259>
- Jiang, Y., Wang, G., & Kamai, T. (2017). Acoustic emission signature of mechanical failure: Insights from ringshear friction experiments on granular materials. *Geophysical Research Letters*, 44(6), 2782–2791. <https://doi.org/10.1002/2016GL071196>
- Johnson, P. A., & Jia, X. (2005). Nonlinear dynamics, granular media and dynamic earthquake triggering. *Nature*, 437(7060), 871–874. <https://doi.org/10.1038/nature04015>
- Jop, P., Forterre, Y., & Pouliquen, O. (2006). A constitutive law for dense granular flows. *Nature*, 441(7094), 727–730. <https://doi.org/10.1038/nature04801>
- Kanamori, H., & Heaton, T. H. (2000). Microscopic and macroscopic physics of earthquakes. In J. Rundle, D. L. Turcotte, & W. Klein (Eds.), *Geocomplexity and the physics of earthquakes* (pp. 147–163). American Geophysical Union.
- Kawamura, H., Hatano, T., Kato, N., Biswas, S., & Chakrabarti, B. K. (2012). Statistical physics of fracture, friction, and earthquakes. *Reviews of Modern Physics*, 84(2), 839–884. <https://doi.org/10.1103/RevModPhys.84.839>
- Kilgore, B. D., Blanpied, M. L., & Dieterich, J. H. (1993). Velocity dependent friction of granite over a wide range of conditions. *Geophysical Research Letters*, 20(10), 903–906. <https://doi.org/10.1029/93GL00368>
- Kohli, A. H., Goldsby, D. L., Hirth, G., & Tullis, T. (2011). Flash weakening of serpentinite at near-seismic slip rates. *Journal of Geophysical Research*, 116(B3), B03202. <https://doi.org/10.1029/2010jb007833>
- Koval, G., Roux, J.-N., Corfdir, A., & Chevoir, F. (2009). Annular shear of cohesionless granular materials: From the inertial to quasistatic regime. *Physical Review E*, 79(2), 021306. <https://doi.org/10.1103/PhysRevE.79.021306>
- Kuwano, O., Ando, R., & Hatano, T. (2013). Crossover from negative to positive shear rate dependence in granular friction. *Geophysical Research Letters*, 40(7), 1295–1299. <https://doi.org/10.1002/grl.50311>
- Kuwano, O., & Hatano, T. (2011). Flash weakening is limited by granular dynamics. *Geophysical Research Letters*, 38(17), L17–L305. <https://doi.org/10.1029/2011GL048530>
- Lachenbruch, A. H. (1980). Frictional heating, fluid pressure, and the resistance to fault motion. *Journal of Geophysical Research*, 85(B11), 6249–6272. <https://doi.org/10.1029/jb085ib11p06097>
- Lee, T. C., & Delaney, P. T. (1987). Frictional heating and pore pressure rise due to a fault slip. *Geophysical Journal of the Royal Astronomical Society*, 88(3), 569–591. <https://doi.org/10.1111/j.1365-246x.1987.tb01647.x>
- Léopoldès, J., Jia, X., Tourin, A., & Mangeney, A. (2020). Triggering granular avalanches with ultrasound. *Physical Review E*, 102(4), 042901. <https://doi.org/10.1103/PhysRevE.102.042901>
- Lim, S. C., & Ashby, M. F. (1987). Wear mechanism maps. *Acta Metallurgica*, 35, 1–24. [https://doi.org/10.1016/0001-6160\(87\)90209-4](https://doi.org/10.1016/0001-6160(87)90209-4)
- Lim, S. C., Ashby, M. F., & Brunton, J. H. (1989). The effects of sliding conditions on the dry friction of metals. *Acta Metallurgica*, 37(3), 767–772. [https://doi.org/10.1016/0001-6160\(89\)90003-5](https://doi.org/10.1016/0001-6160(89)90003-5)
- Lu, K., Brodsky, E. E., & Kavehpour, H. P. (2007). Shear-weakening of the transitional regime for granular flow. *Journal of Fluid Mechanics*, 587, 347–372. <https://doi.org/10.1017/S0022112007007331>
- Ma, S. L., Shimamoto, T., Yao, L., Togo, T., & Kitajima, H. (2014). A rotary-shear low to high-velocity friction apparatus in Beijing to study rock friction at plate to seismic slip rates. *Earthquake Science*, 27(5), 469–497. <https://doi.org/10.1007/s11589-014-0097-5>
- Maddock, R. (1986). Frictional melting in landslide-generated frictionites (hyalomylonites) and fault-generated pseudotachylites—Discussion. *Tectonophysics*, 128(1–2), 151–153. [https://doi.org/10.1016/0040-1951\(86\)90316-1](https://doi.org/10.1016/0040-1951(86)90316-1)
- Magloughlin, J. F., & Spray, J. G. (1992). Frictional melting processes and products in geological-materials—Introduction and discussion. *Tectonophysics*, 204(3–4), 197–206. [https://doi.org/10.1016/0040-1951\(92\)90307-r](https://doi.org/10.1016/0040-1951(92)90307-r)
- Marone, C. (1998). Laboratory-derived friction laws and their application to seismic faulting. *Annual Review of Earth and Planetary Sciences*, 26(1), 643–696. <https://doi.org/10.1146/annurev.earth.26.1.643>
- Mase, C. W., & Smith, L. (1985). Pore-fluid pressures and frictional heating on a fault surface. *Pure and Applied Geophysics*, 122(2–4), 583–607. <https://doi.org/10.1007/bf00874618>
- Mase, C. W., & Smith, L. (1987). Effects of frictional heating on the thermal hydrologic and mechanical response of a fault. *Journal of Geophysical Research*, 92(B7), 6249–6272. <https://doi.org/10.1029/jb092b07p06249>
- McKenzie, D. P., & Brune, J. N. (1972). Melting of fault planes during large earthquakes. *Geophysical Journal of the Royal Astronomical Society*, 29(1), 65–78. <https://doi.org/10.1111/j.1365-246x.1972.tb06152.x>
- McSaveney, M. J., & Davies, T. R. H. (2007). Rockslides and their motion. *Progress in Landslide Science*, 113–133. [https://doi.org/10.1007/978-3-540-70965-7\\_8](https://doi.org/10.1007/978-3-540-70965-7_8)
- Melosh, H. J. (1979). Acoustic fluidization: A new geologic process? *Journal of Geophysical Research*, 84(B13), 7513–7520. <https://doi.org/10.1029/jb084ib13p07513>
- Melosh, H. J. (1996). Dynamical weakening of faults by acoustic fluidization. *Nature*, 379(6566), 601–606. <https://doi.org/10.1038/379601a0>

- Melosh, H. J., & Girdner, K. K. (1995). Rheology of vibrated granular materials: Application to long runout landslides. *EOS Transactions*, 76(46), F270.
- Melosh, H. J., & Ivanov, B. A. (1999). Impact crater collapse. *Annual Review of Earth and Planetary Sciences*, 27(1), 385–415. <https://doi.org/10.1146/annurev.earth.27.1.385>
- Molinari, A., Estrin, Y., & Mercier, S. (1999). Dependence of the coefficient of friction on the sliding conditions in the high velocity range. *Journal of Tribology—Transactions of the ASME*, 121(1), 35–41. <https://doi.org/10.1115/1.2833808>
- Niemeijer, A. R., & Spiers, C. J. (2007). A microphysical model for strong velocity weakening in phyllosilicate-bearing fault gouges. *Journal of Geophysical Research*, 112(B10), B10405. <https://doi.org/10.1029/2007JB005008>
- Noda, H., & Shimamoto, T. (2010). A rate- and state-dependent ductile flow law of polycrystalline halite under large shear strain and implications for transition to brittle deformation. *Geophysical Research Letters*, 37(9), L09310. <https://doi.org/10.1029/2010GL042512>
- Philpotts, A. R. (1964). Origin of pseudotachylites. *American Journal of Science*, 262(8), 1008–1035. <https://doi.org/10.2475/ajs.262.8.1008>
- Putelat, T., Dawes, J. H. P., & Willis, J. R. (2007). Sliding interactions of two frictional interfaces. *Journal of the Mechanics and Physics of Solids*, 55(10), 2073–2105. <https://doi.org/10.1016/j.jmps.2007.03.004>
- Rabinowicz, E. (1951). The nature of the static and kinetic coefficients of friction. *Journal of Applied Physics*, 22(11), 1373–1379. <https://doi.org/10.1063/1.169869>
- Reches, Z., & Lockner, D. A. (2010). Fault weakening and earthquake instability by powder lubrication. *Nature*, 467(7314), 452–455. <https://doi.org/10.1038/nature09348>
- Reinen, L. A., Tullis, T. E., & Weeks, J. D. (1992). Two-mechanism model for frictional sliding of serpentinite. *Geophysical Research Letters*, 19(15), 1535–1538. <https://doi.org/10.1029/92g101388>
- Rempel, A. W., & Rice, J. R. (2006). Thermal pressurization and onset of melting in fault zones. *Journal of Geophysical Research: Solid Earth*, 111(B9), B09314. <https://doi.org/10.1029/2006JB004314>
- Rice, J. R. (1999). Flash heating at asperity contacts and rate dependent friction. *EOS Transactions*, 80, F681.
- Rice, J. R. (2006). Heating and weakening of faults during earthquake slip. *Journal of Geophysical Research*, 111(B5), B05311. <https://doi.org/10.1029/2005JB004006>
- Rice, J. R., & Cocco, M. (2007). Seismic fault rheology and earthquake dynamics. In M. R. Handy (Ed.), *The dynamics of fault zones* (pp. 99–137). MIT Press.
- Rice, J. R., Lapusta, N., & Ranjith, K. (2001). Rate and state dependent friction and the stability of sliding between elastically deformable solids. *Journal of the Mechanics and Physics of Solids*, 49(9), 1865–1898. [https://doi.org/10.1016/S0022-5096\(01\)00042-4](https://doi.org/10.1016/S0022-5096(01)00042-4)
- Rossi, M., Vidal, O., Wunder, B., & Renard, F. (2007). Influence of time, temperature, confining pressure and fluid content on the experimental compaction of spherical grains. *Tectonophysics*, 441(1–4), 47–65. <https://doi.org/10.1016/j.tecto.2007.05.001>
- Rudnicki, J. W., & Rice, J. R. (2006). Effective normal stress alteration due to pore pressure changes induced by dynamic slip propagation on a plane between dissimilar materials. *Journal of Geophysical Research: Solid Earth*, 111(B10), B10308. <https://doi.org/10.1029/2006jb004396>
- Ruina, A. (1983). Slip instability and state variable laws. *Journal of Geophysical Research*, 88(B12), 10359–10370. <https://doi.org/10.1029/JB088iB12p10359>
- Sassa, K., Dang, K., He, B., Takara, K., Inoue, K., & Nagai, O. (2014). A new high-stress undrained ring-shear apparatus and its application to the 1792 Unzen-Mayuyama megaslide in Japan. *Landslides*, 11(5), 827–842. <https://doi.org/10.1007/s10346-014-0501-1>
- Savage, H. M., & Marone, C. (2008). Potential for earthquake triggering from transient deformations. *Journal of Geophysical Research*, 113(B5), B05302. <https://doi.org/10.1029/2007JB005277>
- Savage, S. B. (1984). The mechanics of rapid granular flows. *Advances in Applied Mechanics*, 24, 289–366. [https://doi.org/10.1016/S0065-2156\(08\)70047-4](https://doi.org/10.1016/S0065-2156(08)70047-4)
- Savage, S. B., & Hutter, K. (1989). The motion of a finite mass of granular material down a rough incline. *Journal of Fluid Mechanics*, 199, 177–215. <https://doi.org/10.1017/S0022112089000340>
- Scholz, C. H. (1998). Earthquakes and friction laws. *Nature*, 391(6662), 37–42. <https://doi.org/10.1038/34097>
- Scholz, C. H., & Engelder, J. T. (1976). The role of asperity indentation and ploughing in rock friction, I, Asperity creep and stick-slip. In *International journal of rock mechanics and mining sciences & geomechanics abstracts* (Vol. 13, pp. 149–154). [https://doi.org/10.1016/0148-9062\(76\)90819-6](https://doi.org/10.1016/0148-9062(76)90819-6)
- Scuderi, M. M., Carpenter, B. M., Johnson, P. A., & Marone, C. (2015). Poromechanics of stick-slip frictional sliding and strength recovery on tectonic faults. *Journal of Geophysical Research: Solid Earth*, 120(10), 6895–6912. <https://doi.org/10.1002/2015JB011983>
- Scuderi, M. M., Collettini, C., Viti, C., Tinti, E., & Marone, C. (2017). Evolution of shear fabric in granular fault gouge from stable sliding to stick-slip and implications for fault slip mode. *Geology*, 45(4), 395–398. <https://doi.org/10.1130/G39033.1>
- Shimamoto, T. (1986). Transition between frictional slip and ductile flow for halite shear zones at room temperature. *Science*, 231(4739), 711–714. <https://doi.org/10.1126/science.231.4739.711>
- Shimamoto, T., & Tsutsumi, A. (1994). A new rotary-shear high-speed frictional testing machine: Its basic design and scope of research. *Journal of the Tectonic Research Group of Japan*, 39, 65–78.
- Sibson, R. H. (1975). Generation of pseudotachylite by ancient seismic faulting. *Geophysical Journal of the Royal Astronomical Society*, 43(3), 775–794. <https://doi.org/10.1111/j.1365-246x.1975.tb06195.x>
- Sleep, N. H. (1995). Ductile creep, compaction, and rate and state dependent friction within major fault zones. *Journal of Geophysical Research*, 100(B7), 13065–13080. <https://doi.org/10.1029/94jb03340>
- Swanson, M. T. (1988). Pseudotachylite-bearing strike-slip duplex structures in the Fort Foster brittle zone, S Maine. *Journal of Structural Geology*, 10(8), 813–828. [https://doi.org/10.1016/0191-8141\(88\)90097-1](https://doi.org/10.1016/0191-8141(88)90097-1)
- Taylor, S., & Brodsky, E. E. (2017). Granular temperature measured experimentally in a shear flow by acoustic energy. *Physical Review E*, 96(3), 032913. <https://doi.org/10.1103/PhysRevE.96.032913>
- Tisato, N., Di Toro, G., De Rossi, N., Quaresimin, M., & Candela, T. (2012). Experimental investigation of flash weakening in limestone. *Journal of Structural Geology*, 38, 183–199. <https://doi.org/10.1016/j.jsg.2011.11.017>
- Titone, B., Sayre, K., Di Toro, G., Goldsby, D. L., & Tullis, T. E. (2001). The role of water in the extraordinary frictional weakening of quartz rocks during rapid sustained slip. *EOS Transactions*, 82, T31B–T0841.
- Tullis, T. E. (2007). Friction of rock at earthquake slip rates. *Earthquake Seismology*, 4, 131–152. <https://doi.org/10.1016/B978-044452748-6.00064-X>
- Tullis, T. E., & Weeks, J. D. (1986). Constitutive behavior and stability of frictional sliding of granite. *Pure and Applied Geophysics*, 124, 383–414. <https://doi.org/10.1007/BF00348-602>
- Weeks, J. D. (1993). Constitutive laws for high-velocity frictional sliding and their influence on stress drop during unstable slip. *Journal of Geophysical Research*, 98(B10), 17–637. <https://doi.org/10.1029/93JB00356>

- Weertman, J. (1963). Dislocations moving uniformly on the interface between isotropic media of different elastic properties. *Journal of the Mechanics and Physics of Solids*, 11(3), 197–204. [https://doi.org/10.1016/0022-5096\(63\)90052-8](https://doi.org/10.1016/0022-5096(63)90052-8)
- Weertman, J. (1980). Unstable slippage across a fault that separates elastic media of different elastic constants. *Journal of Geophysical Research*, 85(B3), 1455–1461. <https://doi.org/10.1029/jb085ib03p01455>
- Wenk, H. R. (1978). Are pseudotachylites products of fracture or fusion? *Geology*, 6(8), 507–511. [https://doi.org/10.1130/0091-7613\(1978\)6<507:appofo>2.0.co;2](https://doi.org/10.1130/0091-7613(1978)6<507:appofo>2.0.co;2)
- Xia, K., Rosakis, A. J., Kanamori, H., & Rice, J. R. (2005). Laboratory earthquakes along inhomogeneous faults: Directionality and supershear. *Science*, 308(5722), 681–684. <https://doi.org/10.1126/science.1108193>